

# Scalarized Black Hole dynamics in Einstein dilaton Gauss-Bonnet Gravity

Justin L. Ripley\* and Frans Pretorius†

*Department of Physics, Princeton University, Princeton, New Jersey 08544, USA.*

(Dated: March 18, 2022)

We report on a numerical investigation of the stability of scalarized black holes in Einstein dilaton Gauss-Bonnet (EdGB) gravity in the full dynamical theory, though restricted to spherical symmetry. We find evidence that for sufficiently small curvature-couplings the resulting scalarized black hole solutions are nonlinearly stable. For such small couplings, we show that an elliptic region forms inside these EdGB black hole spacetimes (prior to any curvature singularity), and give evidence that this region remains censored from asymptotic view. However, for coupling values “superextremal” relative to a given black hole mass, an elliptic region forms exterior to the horizon, implying the exterior Cauchy problem is ill-posed in this regime.

## I. INTRODUCTION

We present numerical results on the nonlinear evolution of spherically symmetric black hole solutions in a modified gravity theory: Einstein dilaton Gauss-Bonnet (EdGB) gravity. EdGB gravity is one of the few known scalar tensor theories that may admit sensible classical evolution (at least for some open subsets of initial data; see our earlier studies [1, 2]), yet does not allow the Schwarzschild or Kerr stationary black hole solutions. Instead the expected solutions are conjectured to be “scalarized” black holes [3–5] (the detailed form of this statement depends on the functional form of the Gauss-Bonnet coupling and scalar field potential [6, 7]). The variant of EdGB gravity we consider is poorly constrained by weak field gravity measurements (e.g. from binary pulsars [8]), though to be consistent with the speed of gravitational waves inferred by the binary neutron star merger GW170817 [9] requires a negligible cosmological background for the dilaton field [10]<sup>1</sup>. Assuming the latter, the strongest constraints on the theory may then come from gravitational wave observation of the final moments of binary black hole inspiral. The theory thus provides an interesting alternative to general relativity (GR) to compare against when gravity is in the strong field dynamical regime (see e.g. [12] and references therein).

From the perspective of effective field theory, EdGB gravity can be motivated as the leading correction to GR in a low energy expansion of quantum gravity that incorporates mixing between a scalar degree of freedom and the tensor (metric) degrees of freedom of GR [13, 14]. Then one would not expect significant modifications to GR away from the Planck scale, and in particular not for astrophysical black holes. Alternatively, as we do here, one could consider the coupling parameter of the theory to be arbitrary, and EdGB gravity taken verbatim as a classical theory of gravity with a scale dependent modification to GR. Such a theory may not be mathematically well-posed in some regimes (or in a generic sense not at all [15, 16]), though a “healthy” sector of solutions could still be extracted by treating it as an effective field theory and limiting consideration to small perturbative corrections to GR. Several groups are pursuing such an “order reduction” approach to understanding EdGB gravity, and related theories where beyond-Ricci curvature scalars are added to the Einstein Hilbert gravitational action [12, 17–23]. Another approach, inspired by the Israel-Stewart “fix” of relativistic hydrodynamics [24], is to explicitly modify the GR-extensions to lead to well-posed equations [25, 26].

Our approach is instead to attempt to solve the complete classical field theory, and discover which classes of initial data (if any) lead to well-posed evolution. Our motivation is two fold. The first is the desire to know how classical gravity can in principle differ from the predictions of GR in the dynamical strong field regime, as is applicable to the last stages of binary black hole coalescence. This could give more meaning to quantitative statements of consistency of observed waveforms with the predictions of GR, help constrain EdGB gravity, or discover modifications to GR of a class similar to that offered by EdGB gravity. Though an effective field theory approach as described above is likely “guaranteed”, by construction, to give well-posed evolution schemes for small deviations to GR, it is still unknown if this approach could be pushed to solve for modifications large enough to provide waveforms distinguishable from GR in an observation, given the typical signal-to-noise ratios expected from the current generation of ground based detectors, and taking waveform degeneracies into account.

The second reason is that nonlinear modifications of gravity have been introduced in attempts to address the discovery of dark matter, dark energy, solve the flatness and horizon problems of early universe cosmology, and

\* jripley@princeton.edu

† fpretori@princeton.edu

<sup>1</sup> We note that in asymptotically flat spacetimes it has been explicitly shown that the speed of linearized tensor and scalar perturbations in EdGB gravity approach light speed in regions far away from gravitating sources [11]

resolve the issues of the initial cosmological singularity and singularities formed during gravitational collapse. EdGB is an important and representative member of a class of modified gravity theories, Horndeski theories, that have been invoked to solve these various issues within classical GR (for a recent review on Horndeski theories see [27]), and it thus is interesting to see if the theory is mathematically sensible as a classical field theory.

Previous studies of EdGB black holes have focused on static solutions to the theory (e.g. [5–7]), the dynamics of the EdGB scalar in the *decoupling limit* (e.g. [17, 20, 28]), or linear perturbations of static EdGB black hole backgrounds (e.g. [29]). Additionally, a recent work [22] explored the dynamics of the scalar and metric fields of the theory from an effective-field theory framework. There it was shown that scalarized, rotating EdGB black hole solutions are stable for small enough couplings, up to leading order in metric and scalar field perturbations. Restricted to spherical symmetry, our results extend this to all orders in the Gauss-Bonnet coupling, showing consistency for small couplings, and showing where and how the theory breaks down for large couplings.

In a previous work, we studied the dynamics of EdGB gravity in spherically symmetric collapse using horizon-avoiding coordinates [1, 2]. There we considered collapse of a dense concentration of the dilaton field, and for sufficient mass could show a horizon was forming, though we could not evolve beyond that time. Here, we give results from a new code solving the EdGB equations in horizon penetrating coordinates, allowing us to investigate the long-term stability of scalarized black holes (for times up to of order  $t \sim 10^3 m$ , where  $m$  is the mass of the black hole). Also, we begin with the Schwarzschild solution as initial data (with an optional exterior dilaton field perturbation).

Upon evolution of Schwarzschild initial data, we find that the scalar hair grows, and an elliptic region forms in the interior of the black hole. This indicates black hole physics in EdGB gravity has aspects of it governed by a mixed elliptic-hyperbolic equation (or simply *mixed-type* equation), and it is unclear how this could affect the Cauchy problem exterior to the horizon. I.e., there is no *a-priori* reason to expect this elliptic region to “obey” cosmic censorship, and leave the scalar in the exterior domain to be governed by a hyperbolic partial differential equation (PDE). Instead, we will simply *assume* that this is possible, and *excise* the elliptic region from the domain. If during subsequent evolution no new elliptic region forms, and the solution settles to a stationary state, we will claim this is a self-consistent application of excision, and the resulting hairy black hole is stable (to within limitations of numerical evolution)<sup>2</sup>. We do find this to be the case for Gauss-Bonnet couplings below an extremal limit for a given black hole mass. We compare these solutions to the scalarized decoupled black hole solutions of EdGB gravity, and find good agreement, the better the smaller the Gauss-Bonnet coupling is (for a fixed black hole mass). However, above the extremal limit, an elliptic region does form outside the horizon, indicating a break-down of the exterior Cauchy problem for small black holes (relative to the EdGB coupling scale).

An outline of the rest of the paper is as follows. In Sec. II we describe the equations of motion, variables, and metric ansatz we use. In Sec. III we describe aspects of the numerical code, including our excision strategy, as well as some diagnostic quantities we monitor. In Sec. IV we describe the results mentioned above in detail, and end in Sec. V with concluding remarks. We leave some convergence results, and a derivation of the decoupling limit about a Schwarzschild black hole in Painlevé-Gullstrand coordinates, to the appendices. We use geometric units ( $8\pi G = 1$ ,  $c = 1$ ) and follow the conventions of Misner, Thorne, and Wheeler [31].

## II. EQUATIONS OF MOTION

The action for the EdGB gravity theory we consider is

$$S = \frac{1}{2} \int d^4x \sqrt{-g} (R - (\nabla\phi)^2 + 2\lambda f(\phi)\mathcal{G}), \quad (1)$$

where  $f(\phi)$  is a (so far unspecified) function, and  $\mathcal{G}$  is the Gauss-Bonnet scalar

$$\mathcal{G} \equiv \frac{1}{4} \delta_{\rho\sigma\gamma\delta}^{\mu\nu\alpha\beta} R^{\rho\sigma}{}_{\mu\nu} R^{\gamma\delta}{}_{\alpha\beta}, \quad (2)$$

where  $\delta_{\rho\sigma\gamma\delta}^{\mu\nu\alpha\beta}$  is the generalized Kronecker delta. In geometric units, the Gauss-Bonnet coupling constant  $\lambda$  has dimensions length squared. Varying (1) with respect to the metric and scalar fields, the EdGB equations of motion are

$$E_{\mu\nu}^{(g)} \equiv R_{\mu\nu} - \frac{1}{2} g_{\mu\nu} R + 2\lambda \delta_{\alpha\beta\rho\sigma}^{\gamma\delta\kappa\lambda} R^{\rho\sigma}{}_{\kappa\lambda} (\nabla^\alpha \nabla_\gamma f(\phi)) \delta^\beta_{(\mu} g_{\nu)\delta} - T_{\mu\nu} = 0, \quad (3a)$$

---

<sup>2</sup> Also in this case, that we can freely specify the initial data for all characteristics is not in contradiction with the result of Morawetz on the Tricomi mixed-type equation [30], which seems the relevant mixed-type equation for EdGB gravity here [2]; rather, following the excision philosophy, we simply do not care what irregularities or lack of uniqueness occur in the interior of the excised region.

$$\begin{aligned}
T_{\mu\nu} &= \nabla_\mu \phi \nabla_\nu \phi - \frac{1}{2} g_{\mu\nu} (\nabla \phi)^2, \\
E^{(\phi)} &\equiv \nabla_\mu \nabla^\mu \phi + \lambda f'(\phi) \mathcal{G} = 0.
\end{aligned}
\tag{3b}$$

In this work we will only consider the coupling function

$$f(\phi) = \phi. \tag{4}$$

While other coupling functions are often considered in the literature on EdGB black holes, this is the simplest which is thought to give rise to stable scalarized black hole solution; see [3, 5, 17, 20, 32] and references therein. This coupling may additionally be motivated as the lowest order term in the effective field theory expansion of a metric theory coupled to a scalar field (e.g. [8]). From the symmetry  $\lambda \rightarrow -\lambda, \phi \rightarrow -\phi$ , we only consider  $\lambda \geq 0$ .

We evolve this system in Painlevé-Gullstrand (PG)-like coordinates (e.g. [33–36])

$$ds^2 = -\alpha(t, r)^2 dt^2 + (dr + \alpha(t, r) \zeta(t, r) dt)^2 + r^2 (d\vartheta^2 + \sin^2 \vartheta d\phi^2), \tag{5}$$

so-named since  $t = \text{const.}$  cross sections are spatially flat (the Schwarzschild black hole in these coordinates is given by  $\alpha = 1, \zeta = \sqrt{2m/r}$ ).

We define the variables

$$Q \equiv \partial_r \phi, \tag{6a}$$

$$P \equiv \frac{1}{\alpha} \partial_t \phi - \zeta Q, \tag{6b}$$

and take algebraic combinations of Eq. (3b) and the  $tr$ ,  $rr$ , and  $\vartheta\vartheta$  components of Eq. (3a) (c.f. [2]) to obtain the following evolution equation for the  $\{P, Q\}$  variables:

$$E_{(Q)} \equiv \partial_t Q - \partial_r (\alpha [P + \zeta Q]) = 0, \tag{7a}$$

$$E_{(P)} \equiv \mathcal{A}_{(P)} \partial_t P + \mathcal{F}_{(P)} = 0. \tag{7b}$$

The quantities  $\mathcal{A}_{(P)}$  and  $\mathcal{F}_{(P)}$  are lengthy expressions of  $\{\alpha, \zeta, P, Q\}$  and their radial derivatives. We present their explicit forms in Appendix C. In the limit  $\lambda = 0$  Eq. (7b) reduces to

$$\partial_t P - \frac{1}{r^2} \partial_r (r^2 \alpha [Q + \zeta P]) = 0. \tag{8}$$

Interestingly, in PG coordinates the Hamiltonian and momentum constraints do not change their character as elliptic differential equations going from GR to EdGB gravity:

$$E_{\mu\nu}^{(g)} n^\mu n^\nu \propto \partial_r ((r - 8\lambda f' Q) \alpha^2 \zeta^2) - 8\lambda f' \frac{P}{\alpha} \partial_r (\alpha^3 \zeta^3) - r^2 \alpha^2 \rho = 0, \tag{9a}$$

$$\begin{aligned}
E_{\mu r}^{(g)} n^\mu &\propto \left( 1 - 8\lambda f' \frac{\zeta}{r} P - 8\lambda f' \frac{Q}{r} \right) \zeta \partial_r \alpha - \frac{1}{2} r \alpha j_r \\
&+ 2\lambda f' \frac{Q}{r \alpha^2} \partial_r (\alpha^2 \zeta^2) + 4\lambda \frac{\zeta}{r} \partial_r (f' P) = 0,
\end{aligned}
\tag{9b}$$

where

$$\rho \equiv n^\mu n^\nu T_{\mu\nu} = \frac{1}{2} (P^2 + Q^2), \tag{10a}$$

$$j_r \equiv -\gamma_r^\mu n^\nu T_{\mu\nu} = -PQ, \tag{10b}$$

$f' \equiv df/d\phi$ , and  $n_\mu \equiv (-\alpha, 0, 0, 0)$ . While Eqs. (9a) and (9b) hold for any  $f$ , as mentioned above we only consider  $f(\phi) = \phi$  in this article.

### III. DESCRIPTION OF CODE AND SIMULATIONS

#### A. Diagnostics

As PG coordinates are spatially flat the Arnowitt-Deser-Misner mass prescription always evaluates to zero, and does not capture the correct physical mass of the spacetime. Instead then we use the Misner-Sharp mass [37]

$$m_{MS}(t, r) = \frac{r}{2} (1 - (\nabla r)^2) = \frac{r}{2} \zeta(t, r)^2. \tag{11}$$

evaluated at spatial infinity to define the spacetime mass (and this does give the correct mass for the Schwarzschild solution in GR)

$$m \equiv \lim_{r \rightarrow \infty} m_{MS}(t, r). \quad (12)$$

The Misner-Sharp mass can be thought of as the charge associated with the Kodama current, which is conserved in any spherically symmetric spacetime (regardless of whether the Einstein equations hold) [38–40]. Going through this “derivation” of the Misner-Sharp mass, we find that we can think of  $m_{MS}(t, r)$  as representing the radially integrated energy density of the following (conserved) stress-energy tensor for EdGB gravity [2]

$$\mathcal{T}_{\mu\nu} \equiv -2\lambda \delta_{\alpha\beta\rho\sigma}^{\gamma\delta\kappa\lambda} R^{\rho\sigma}{}_{\kappa\lambda} (\nabla^\alpha \nabla_\gamma \phi) \delta_{(\mu}^\beta g_{\nu)\delta} + \nabla_\mu \nabla_\nu \phi - \frac{1}{2} g_{\mu\nu} (\nabla\phi)^2. \quad (13)$$

There is no other definition for a covariantly conserved stress-energy tensor that does not involve both the Riemann tensor and derivatives of the scalar field (besides the Einstein tensor itself, or a constant times the stress-energy tensor) in EdGB gravity. We note that the stress-energy tensor 13 also conforms with earlier choices for the stress-energy tensor of EdGB gravity [3].

As described in the next section we compactify so that infinity is at a finite location on our computational grid. The asymptotic mass  $m$  is preserved up to truncation error in our simulations of both EdGB gravity and GR. Given a spacetime with mass  $m$ , we define the dimensionless curvature-coupling

$$C \equiv \frac{\lambda}{m^2}. \quad (14)$$

We will classify different solutions based on their curvature couplings  $C$ , with GR the limit  $C = 0$ ; empirically (as we discuss in our results IV) we find strong EdGB corrections arising when  $C \gtrsim 0.1$ .

Following the procedure used in [1, 2], we calculate the radial characteristics of the scalar degree of freedom via Eqs. (7a) and (7b), after having removed the spatial derivatives of  $\alpha$  and  $\zeta$  from these equations using the constraints (9a, 9b). The corresponding characteristic speeds  $c_\pm$  are

$$c_\pm \equiv \mp \xi_t / \xi_r, \quad (15)$$

where  $\xi_a \equiv (\xi_t, \xi_r)$  solves the characteristic equation

$$\det \left[ \begin{pmatrix} \delta E_{(P)} / \delta (\partial_a P) & \delta E_{(P)} / \delta (\partial_a Q) \\ \delta E_{(Q)} / \delta (\partial_a P) & \delta E_{(Q)} / \delta (\partial_a Q) \end{pmatrix} \xi_a \right] = 0. \quad (16)$$

In the limit  $\lambda = 0$ , these speeds reduce to the radial null characteristic speeds in PG coordinates  $c_\pm^{(n)}$

$$c_\pm^{(n)} \equiv \alpha (\pm 1 - \zeta). \quad (17)$$

We see that  $\zeta = 1$  marks the location of a marginally outer trapped surface (MOTS) (e.g. [41] and references therein). We take the location of the MOTS to represent the size of the black hole on any given time slice.

The characteristic equation, Eq. (16), takes the following form when expressed as an equation for the characteristic speeds  $c$

$$\mathcal{A}c^2 + \mathcal{B}c + \mathcal{C} = 0, \quad (18)$$

where

$$\mathcal{A} \equiv \frac{\delta E_{(P)}}{\delta (\partial_t P)} \frac{\delta E_{(Q)}}{\delta (\partial_t Q)} - \frac{\delta E_{(P)}}{\delta (\partial_t Q)} \frac{\delta E_{(Q)}}{\delta (\partial_t P)}, \quad (19a)$$

$$\mathcal{B} \equiv - \left( \frac{\delta E_{(P)}}{\delta (\partial_t P)} \frac{\delta E_{(Q)}}{\delta (\partial_r Q)} - \frac{\delta E_{(P)}}{\delta (\partial_t Q)} \frac{\delta E_{(Q)}}{\delta (\partial_r P)} \right) - \left( \frac{\delta E_{(P)}}{\delta (\partial_r P)} \frac{\delta E_{(Q)}}{\delta (\partial_t Q)} - \frac{\delta E_{(P)}}{\delta (\partial_r Q)} \frac{\delta E_{(Q)}}{\delta (\partial_t P)} \right), \quad (19b)$$

$$\mathcal{C} \equiv \frac{\delta E_{(P)}}{\delta (\partial_r P)} \frac{\delta E_{(Q)}}{\delta (\partial_r Q)} - \frac{\delta E_{(P)}}{\delta (\partial_r Q)} \frac{\delta E_{(Q)}}{\delta (\partial_r P)}. \quad (19c)$$

Where the discriminant  $\mathcal{D} \equiv \mathcal{B}^2 - 4\mathcal{A}\mathcal{C} > 0$  are regions of spacetime where the equations are hyperbolic, where  $\mathcal{D} < 0$  the equations are elliptic, and following the language of mixed-type PDEs (e.g. [42] and references therein), the co-dimension one surfaces where  $\mathcal{D} = 0$  separating elliptic and hyperbolic regions are called sonic lines. In the

GR limit  $\lambda = 0$  the scalar equations are always hyperbolic ( $\mathcal{D} > 0$ ), though as we found in [1, 2], for sufficiently strong couplings  $C$  the discriminant  $\mathcal{D}$  is not of definite sign, and the scalar equations are then of mixed-type (similar conclusions have been drawn for other member of the Horndeski class of theories; see e.g. [43–45]). As we are working in spherical symmetry, the tensor degrees of freedom are pure gauge. Our hyperbolicity analysis can thus be thought of as applying to the scalar “sector” of EdGB gravity.<sup>3</sup>

## B. Spatial compactification

In vacuum when  $P = Q = 0$ , the general solution to Eqs. (9a) and (9b) is  $\zeta \propto r^{-1/2}$  and  $\alpha = \text{const.}$ <sup>4</sup> We found that this falloff in  $\zeta$  made it difficult to impose stable outer boundary conditions at a fixed, finite  $r$ . To alleviate this problem, we spatially compactify through a stereographic projection

$$r \equiv \frac{x}{1 - x/L}, \quad (20)$$

where  $L$  is a constant, and discretize along a uniform grid in  $x$ , with spatial infinity  $x = L$  now the outer boundary of our computational domain. For all the simulations presented in this article we chose  $L = 5m$ , where  $m$  is the mass of the initial Schwarzschild black hole. At  $x = L$  we impose the conditions  $\alpha|_{x=L} = 1$ ,  $\zeta|_{x=L} = 0$ ,  $P|_{x=L} = 0$ ,  $Q|_{x=L} = 0$ ,  $\phi|_{x=L} = 0$ . These conditions are consistent with our initial conditions and asymptotic fall off of the metric and scalar field. For the latter, generally  $\phi \rightarrow 1/r$ , though if we impose exact Schwarzschild initial data outside some radius  $r_1$  (such that  $\phi(r > r_1, t = 0) = 0$  and  $\partial_t \phi(r > r_1, t = 0) = 0$ ), the Gauss-Bonnet curvature will source an asymptotic field that decays like  $1/r^4$ ; by causality (as long as the equations are hyperbolic) the  $1/r$  component sourced by the black hole, or any scalar radiation from a field we put in at  $r < r_1$ , will never reach spatial infinity.

## C. Initial data

The computational domain covers  $x \in [x_{exc}, L]$  ( $r \in [r_{exc}, \infty)$ ), where  $x_{exc}$  ( $r_{exc}$ ) is the excision radius, and can vary with time (described in the following section). We set initial data at  $t = 0$  by specifying the values of  $P$  and  $Q$ , and then solve for  $\alpha$  and  $\zeta$  using the momentum and Hamiltonian constraints. These ordinary differential equations (ODEs) are discretized using the trapezoid rule and solved with a Newton relaxation method, integrating from  $x = x_{exc}$  to  $x = L$ . At  $x = x_{exc}$  (some distance inside the horizon, as discussed in the next section) we set  $\alpha$  and  $\zeta$  to their Schwarzschild values:

$$\alpha|_{t=0, x=x_{exc}} = 1, \quad \zeta|_{t=0, x=x_{exc}} = \sqrt{\frac{2m}{r(x_{exc})}}. \quad (21)$$

If we begin with zero scalar field energy ( $Q|_{t=0} = P|_{t=0} = 0$ ), solving the constraints recovers the Schwarzschild solution on  $t = 0$  to within truncation error.

## D. Excision

At every time step we solve for  $\alpha$ ,  $\zeta$ ,  $P$ , and  $Q$  by alternating between an iterative Crank-Nicolson solver for  $P$  and  $Q$  and the ODE solvers for  $\alpha$  and  $\zeta$ , until the discrete infinity norm of all the residuals are below a pre-defined tolerance (typically the tolerance was  $\lesssim 10^{-10}$ , smaller than the typically size of the one-norm of the independent residuals. This strategy is a similar strategy to that used in our earlier code based on Schwarzschild-like coordinates, and more details can be found in [2]). The excision strategy assumes all characteristics of hyperbolic equations are pointing out of the domain at the excision surface  $x = x_{exc}$ . This implies that for  $P$  and  $Q$  we cannot set boundary conditions there, rather their evolution equations must be solved, with the finite difference stencils for the radial derivatives appropriately changed to one-sided differences. For  $\alpha$ , as with the initial data, the inner boundary condition is arbitrary, and after each iteration we rescale it so that  $\alpha(t, x = L) = 1$ . For  $\zeta$ , to obtain a consistent solution to the

<sup>3</sup> Note that in a less symmetrical spacetime more care would need to be taken to distinguish between scalar and tensor dynamics due to the derivative coupling between the scalar and metric fields in the EdGB equations of motion; see Eqs. 3.

<sup>4</sup> In EdGB gravity curvature always sources a scalar field, though for  $r \gg m$  for an isolated source in an asymptotically flat spacetime, the fall off of the curvature-sourced scalar field is sufficiently fast not to alter, through back reaction, the fall off of the metric derived when  $P = Q = 0$ .

full field equations requires that the boundary condition  $\zeta(t, x = x_{exc})$  be set by solving the corresponding evolution equation for  $\zeta$  there (optionally  $\zeta$  could be evolved over the entire domain using this equation). Taking algebraic combinations of the equations of motion (3a), an appropriate evolution equation for  $\zeta$  can be obtained

$$\mathcal{A}_{(\zeta)}\partial_t\zeta + \mathcal{F}_{(\zeta)} = 0, \quad (22)$$

The expressions for  $\mathcal{A}_{(P)}$  and  $\mathcal{F}_{(P)}$  are lengthy expressions of  $\lambda$ ,  $\{\alpha, \zeta, P, Q\}$ , and their radial derivatives. We defer showing their full form to Appendix C. In the limit  $\lambda = 0$ , Eq. (22) reduces to

$$\partial_t\zeta - \alpha\zeta\partial_r\zeta - \frac{\alpha}{2r}\zeta^2 - \frac{r}{2\zeta}T_{tr} = 0. \quad (23)$$

Eq. (22) provides the boundary condition for  $\zeta$  at the excision surface. We then integrate outwards in  $r$  using the Hamiltonian constraint, Eq. (9a) as described above to solve for  $\zeta$ .

The formation of a MOTS is signaled by  $\zeta = 1$  (Eq. (17)), and we always place the excision surface inside the MOTS<sup>5</sup>. The location of  $x_{exc}$  is updated every time step before solving for the scalar and metric fields. The location of the excision point is chosen so that it is always interior to the MOTS, but lies exterior to (or directly on) the sonic line (for further discussion see Sec. III A and Sec. IV D). The location for  $r_{exc}$  on our initial data slice depended on the strength of the curvature coupling  $C$ , which we detail in our Results, Sec. IV.

### E. Fixed mesh refinement with a hyperbolic-ODE system

To achieve the necessary long term accuracy over thousands of  $m$  in evolution using limited computational resources, we evolved some simulations using a Berger and Oliger (BO) style mesh refinement algorithm [46]. Due to the nature of our initial data and perturbations, a fixed hierarchy suffices, with the higher resolution meshes confined to smaller volumes centered about the origin. For those runs, we typically used 4 additional levels beyond the base (coarsest) level, with a 2 : 1 refinement ratio between levels; specifically, we set the inner boundary for all levels at  $x_{exc}$ , and the outer refinement boundary locations at  $x_l/m = \{5.00, 2.30, 2.00, 1.75, 1.55\}$ , from coarsest to finest (the initial horizon location  $r = 2m$ , and we chose the excision radius  $x_{exc}$  so that  $r_{exc}(x_{exc}) = 0.8 \times 2m$ ; see Eq. (20)).

The original BO algorithm was designed for purely hyperbolic systems of equations; to include the ODE constraint equations, we employ the *extrapolation and delayed solution* modification developed for such coupled elliptic/hyperbolic systems [47]. Here, for the hyperbolic equations (governing  $P$  and  $Q$ ), the solution is obtained on the mesh hierarchy with the usual BO time-stepping procedure : one time step is first taken on a coarse *parent* level before two<sup>6</sup> steps are taken on the next finer *child* level, and this is repeated recursively down the mesh hierarchy. During this phase the ODEs are not solved, and where the values of the corresponding constrained variables ( $\alpha$  and  $\zeta$ ) are needed to evaluate terms in the hyperbolic equations, approximations for these variables are obtained via extrapolation from earlier time levels. Instead, the ODEs are solved after the fine-to-coarse level injection phase of the hyperbolic variables, when the advanced time of a given parent level is in sync with all overlapping child levels (thus, on the very finest level this scheme reduces to the unigrid algorithm described in the previous section). For more details see [47].

One difference with our system of equations compared to that described in [47], is there some form of global relaxation method was assumed for the elliptics, while here the ODE nature of our constraint equations requires integration from the inner to outer boundary. This might complicate things for a general hierarchy with disconnect grids on a given level. Here, since we only have one grid per level, and each always includes the physical inner boundary, it is reasonably straight forward to integrate the ODEs during the solution phase of the algorithm (see also section 6.7 of [48]): we begin on the finest level, setting the boundary conditions as required at  $x = x_{exc}$ , then integrate outward, using the solution at the last point on a child level as an initial condition for continued integration on the parent level (with the solution at interior points on the child level injected to common points on the parent level). This is schematically shown for two levels in Fig. 1. For  $\zeta$ , the boundary condition at  $x = x_{exc}$  is obtained by its corresponding evolution equation as described in the previous section;  $\alpha$  at  $x = x_{exc}$  is set by extrapolation from prior time levels, and we only globally rescale  $\alpha$  to satisfy our outer boundary condition  $\alpha(t, x = L) = 1$  at times when all levels of the hierarchy are in sync.

<sup>5</sup> In all cases we have considered we find that the “characteristic horizon” (the location where  $c_+ < 0$  for the EdGB scalar field) is exterior to the MOTS, so placing the excision point interior to the MOTS should lead to well posed evolution, provided the equations of motion for the EdGB scalar remain hyperbolic.

<sup>6</sup> because of our 2 : 1 refinement ratio in space and time.



FIG. 1: Schematic illustration of the solution of ODEs at synchronized levels with fixed mesh refinement in our setup: we integrate from left to right (the compactified radial coordinate  $x$  increases from left to right).

Figure	grid layout	grid resolution $\Delta x$	CFL number	initial data
2,3,4,5,6,12	fixed mesh refinement	0.38	0.25	Schwarzschild
7	unigrid	0.024	0.5	Schwarzschild with bump: $\phi_0 = 0.1, a = 45, b = 55.$
8	unigrid	0.012	0.2 and 0.1	Schwarzschild
9	unigrid	0.049	0.2	Schwarzschild
10	unigrid	0.049	0.4	Schwarzschild
11	unigrid	0.012	0.2	Schwarzschild

TABLE I: Simulation parameters. Grid resolution  $\Delta x$  refers to the base grid resolution for the fixed mesh refinement runs. A discussion of Schwarzschild initial data can be found in Sec. IV B, and a discussion of “Schwarzschild with bump” initial data can be found in Sec. IV C. See also Sec. IV A.

## IV. SCALARIZED BLACK HOLES: NUMERICAL RESULTS

### A. Overview of simulations and plots

To help keep track of the various simulation results we present, we collect some of our simulation parameters in Table. (I). We found for long time evolution simulations ( $t \gtrsim 10^3 m$ ) fixed mesh refinement was essential to maintain high accuracy evolution ( $\delta m/m \lesssim 10^{-2}$ ). Unigrid evolution was sufficient for shorter simulation runs. When we quote a value of resolution  $\Delta x$ , it represents the resolution of the coarsest (base) level if fixed mesh refinement was used, otherwise it is the resolution of the unigrid mesh. We found that stably resolving the initial growth of the sonic line that formed inside the EdGB black hole required using smaller Courant-Friedrichs-Lewy (CFL) numbers, but CFL numbers as large as 0.5 led to stable evolution if we excised well away from the sonic line.

### B. Growth of “hair” from Schwarzschild initial data

For most of our simulations we begin with a ( $t = \text{const.}$ ) slice of the Schwarzschild black hole solution in PG coordinates; which is (as is any spacelike slice of Schwarzschild) an *exact* solution to the initial value problem in EdGB gravity. Specifically, at  $t = 0$ , for  $x > x_{exc}$  (the initial excision radius as described in Sec. III D), we set

$$\phi|_{t=0} = 0, \quad Q|_{t=0} = 0, \quad P|_{t=0} = 0, \quad \alpha|_{t=0} = 1, \quad \zeta|_{t=0} = \sqrt{\frac{2m}{r(x)}}. \quad (24)$$

We then evolve this, performing a survey of outcomes varying the EdGB coupling parameter  $\lambda$  (in the GR case  $\lambda = 0$ , as expected, the resultant numerical solution is static to within truncation error).

Previous studies of static scalarized black hole solutions in EdGB gravity have found that regularity of the scalar field at the horizon places an upper limit on the coupling parameter. For the linear coupling case we consider, this is (see e.g.[5])

$$\frac{\lambda}{r_h^2} \leq (192)^{-1/2} \approx 0.07, \quad (25)$$

where  $r_h$  is the areal radius of the horizon. For black holes much larger than this,  $r_h \approx 2m$  (the space time is close to Schwarzschild), though approaching the extremal limit a non-negligible amount of the spacetime mass  $m$  can be

contained in the scalar field, and simply replacing  $r_h$  with  $2m$  to express the above in terms of our curvature-coupling parameter  $C$  (14) gives a poor estimate of the corresponding extremal value  $C_{extr}$ . From Figure 4 of [5] we can infer a more accurate translation :

$$C \leq C_{extr} \approx 0.22. \quad (26)$$

We find the extremal limit is not characterized by the appearance of a naked curvature singularity, but instead the formation of a sonic line (and elliptic region) outside of the horizon of the black hole. Our measured extremal limit of  $C_{extr} \sim 0.23$ , as shown in Sec. IV D, is quite close to the above limit from [5].

Note that the “extremal limit” for a scalarized EdGB black hole is of a different nature than the extremal limits of Kerr or Reissner-Nordstrom black holes. The spin or electric charge of a black hole is set by the black hole’s formation history: black holes of the same mass can have different spins or charges depending on the initial configuration and net charge and angular momentum of the matter that fell in to form the black hole. By contrast for an EdGB black hole the final scalar charge is set by the Gauss-Bonnet coupling, and Gauss-Bonnet curvature at the horizon, independent of its formation history [3, 5].

Given that the Schwarzschild solution, of any mass, is valid initial data in EdGB gravity, we can certainly begin with superextremal black holes in our evolution (and again to be clear, here we use the term “superextremal” to refer to  $C > C_{extr}$ ; there is no spin or charge in our numerical solutions). As we show below however, these develop elliptic regions outside the horizon. Moreover, our results in [1, 2] show that trying to form a superextremal black hole from gravitational collapse of the dilaton field (in spherical symmetry) will result in an elliptic region appearing before a horizon. This suggests superextremal black holes in EdGB gravity exist in the regime of the theory governed by mixed-type equations, and their presence or “formation” (however that could be interpreted in a mixed-type problem) would mark a breakdown of the Cauchy problem. Also note that failure of the Cauchy problem is not *a priori* connected to regions of strong curvature or black hole formation; as further shown in [1, 2], strong coupling and mixed-type character can be present for arbitrarily small spacetime curvature.

We first present results from evolution of Schwarzschild black hole initial data, and curvature couplings below the extremal limit. In all cases, if we move our excision radius sufficiently far interior to the horizon, we find that at some time an elliptic region forms in the interior. However, for these cases we can choose an excision radius closer to the horizon so that the evolution settles to a stationary state without any elliptic region forming in this new domain. As discussed in the introduction, we view this as a consistent initial boundary value evolution of EdGB gravity where the elliptic region is “censored” from the exterior hyperbolic region. In Figs. 2 and 3 we show examples of scalar hair growth for these cases (with the elliptic region excised), and their difference from the static “decoupled” scalar field profiles for a Schwarzschild black hole background (see Appendix B), for various curvature-couplings. These runs employed the fixed mesh refinement algorithm described above, with the base level grid having  $\Delta x = 0.39$  resolution, Courant-Friedrichs-Lewy (CFL) number of 0.25, and an excision radius at fixed at  $r_{exc} = 0.95 \times 2m$ . We find the scalar field settles down to solutions that differ little from the static decoupled scalar field profile, although the difference grows as the curvature coupling approaches the extremal limit (c.f. Fig. 3 of [5]). Nevertheless, in agreement with the results of [5], the difference of the full solution from the static decoupled limit solution remains small outside the black hole horizon. From convergence studies we find we can resolve the difference of the scalar field profile from its decoupled value well within truncation error; see Fig. 4. For the case  $C = 0.16$ , in Fig. 5 we show growth of Ricci curvature sourced by the scalar field, and in Fig. 6 a corresponding plot of convergence and estimated truncation error in  $R$ .

### C. Perturbed Schwarzschild initial data

Schwarzschild initial data is not generic; in particular, the scalar field is (initially) only growing in response to the Gauss-Bonnet curvature source. To investigate a slightly broader class of initial conditions, here we add a small, mostly ingoing propagating perturbation to  $\phi$  outside the horizon:

$$\phi(t, r)|_{t=0} = \begin{cases} \phi_0 \exp\left[-\frac{1}{(r-a)(b-r)}\right] \exp\left[-5\left(\frac{r-(a+b)/2}{a+b}\right)^2\right] & a < r < b \\ 0 & \text{otherwise} \end{cases}, \quad (27a)$$

$$Q(t, r)|_{t=0} = \partial_r \phi(t, r)|_{t=0}, \quad (27b)$$

$$P(t, r)|_{t=0} = 0. \quad (27c)$$

This family of initial data (rescaled “bump functions” multiplied by a Gaussian) is smooth and compactly supported outside the initial black hole horizon for  $a > 2m$ . With a fixed curvature-coupling  $C$ , we find that we can stably



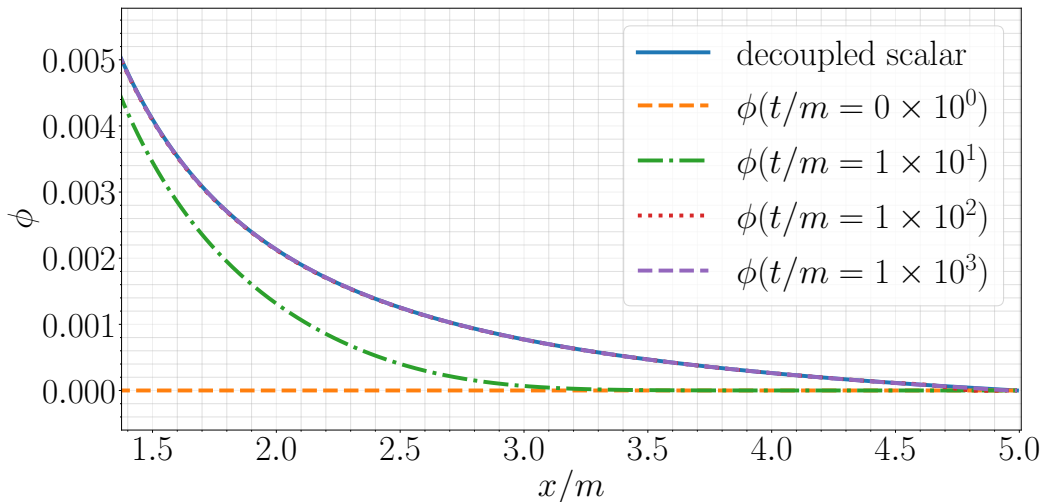
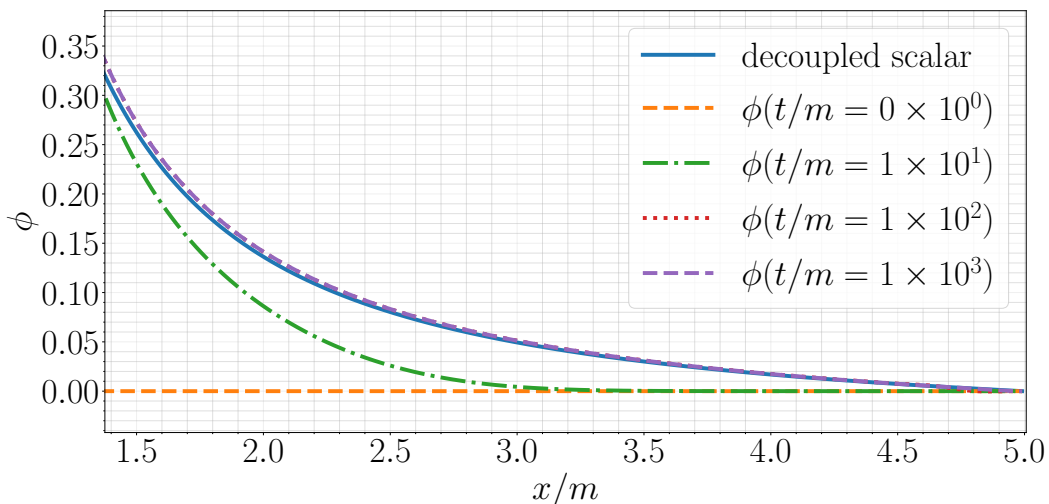
(a)  $C = 2.5 \times 10^{-3}$ (b)  $C = 0.16$ 

FIG. 2: Growth of scalar “hair” from Schwarzschild initial data. Shown is the scalar field profile at several times during an evolution for two different cases of the curvature coupling  $C$  (14); the extremal limit (see the discussion in Sec. IV B) is  $C_{extr} \approx 0.23$ . The horizon (MOTS) is located at  $x_h/m \approx 1.48$ , and spatial infinity is at  $x/m = 5$ .

Notice the different range of scales on the y-axis of each figure. Also shown for comparison is the estimate of the final profile using the decoupled scalar approximation (Appendix B); see also Fig.3. For simulation parameters see Table. I.

evolve an initial black hole plus scalar field bump if the amplitude of the latter is sufficiently small; or equivalently if the metric curvature measured by the Ricci scalar  $R$  induced by the scalar field bump is sufficiently small. For our initial data for  $\alpha$  and  $\zeta$ , we set their values at the excision surface as in Eq. (24), and then integrate outwards in  $r$ . An example of such a case is shown in Fig. 7. When the induced curvature is large, an elliptic region forms outside the black hole horizon (and soon after that the code crashes). As a rough estimate, we find this occurs when  $|R \times \lambda|_\infty \gtrsim 0.1$ . This result is consistent with our earlier findings of collapse of a scalar field pulse without any interior black hole [1, 2].

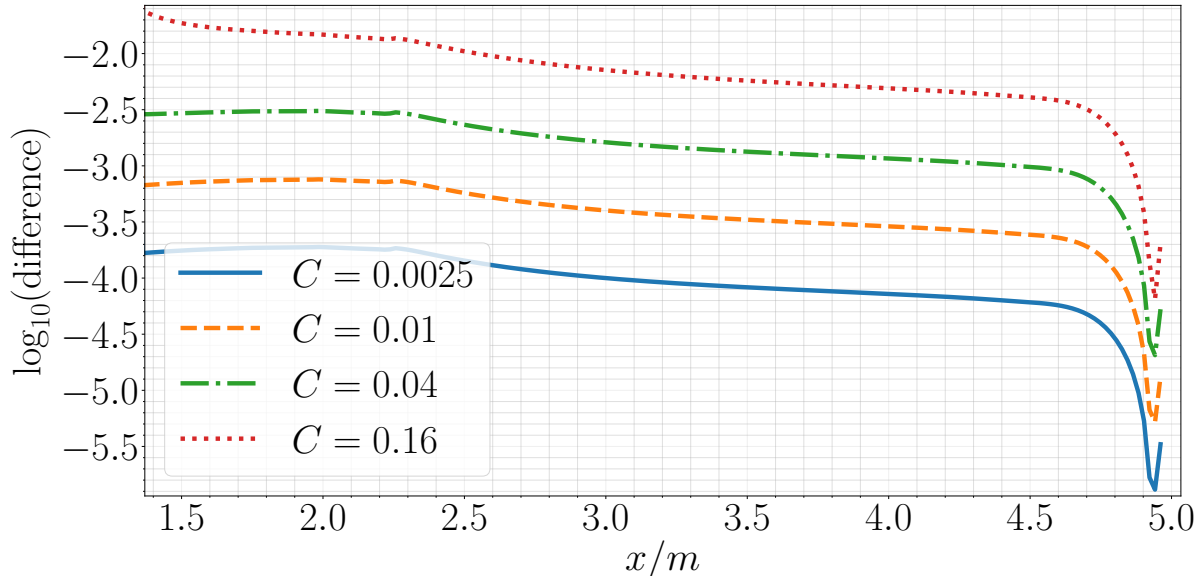


FIG. 3: Difference between the late time ( $t \sim 2000m$ ) scalar field profile obtained from the non-linear simulations to that of the decoupled estimate (see Appendix B), for several values of the curvature coupling  $C$ ; see also Fig. 2. The black hole horizon (MOTS) is at  $x/m \approx 1.48$ , and spatial infinity is at  $x/m = 5$ . As expected, the decoupling limit approximation improves the further  $C$  is away from the extremal limit  $C_{extr} \sim 0.23$ . For simulation parameters see Table. I.

#### D. Internal structure of an EdGB black hole, and the near extremal limit

For small values of the curvature coupling we can consistently excise any elliptic region that forms interior to the horizon. We always excise the Schwarzschild curvature singularity at  $r = 0$ , and in none of the cases we have run (small or large curvature coupling) do we see any signs of a curvature or scalar field singularity forming away from  $r = 0$  while the equations remain hyperbolic. We can typically evolve for some time after an elliptic region forms without excising it before the code crashes, however this as an artifact of finite resolution, and we can only expect convergence to the continuum limit using our hyperbolic scheme until the first appearance of the sonic line. In other words, to say anything rigorous about what might occur within the elliptic region would require solving a mixed-type problem, and we do not have the tools for doing so.

With increasing values of the curvature coupling approaching the extremal limit (26), as the scalar field grows, the location at which the sonic line first appears moves closer to the MOTS. Prior to this, we excise some distance within the MOTS, though when the sonic line appears we increase the excision radius to be at the sonic line<sup>7</sup>. We then employ a “high water mark” strategy during subsequent evolution, increasing the excision radius to match the location of the sonic line if it grows, though do not reduce the excision radius if the sonic line shrinks (presumed to be happening if the characteristic discriminant on the excision boundary increases in magnitude away from zero).

For cases where the elliptic region remains censored, we typically find that initially the sonic line does grow, and then (presumably) shrinks within the excision radius as the solution settles to a stationary state. For interest, we estimate the location of the sonic line by extrapolation, as follows. Recall, the equation for the radial characteristics is (Eq. (16))

$$\mathcal{A}c^2 + \mathcal{B}c + \mathcal{C} = 0, \quad (28)$$

where  $\mathcal{A}, \mathcal{B}, \mathcal{C}$  are functions of  $\alpha, \zeta, P, Q$ , and their radial derivatives. The characteristics thus satisfy

$$c_{\pm} = \frac{1}{2\mathcal{A}} \left( -\mathcal{B} \pm \sqrt{\mathcal{B}^2 - 4\mathcal{A}\mathcal{C}} \right), \quad (29)$$

<sup>7</sup> The scalar and null characteristics are generally different from each other in EdGB gravity. For our excision strategy to be stable, we require all of the metric and scalar characteristics to point into the excised region. In all cases we have studied, the scalar characteristics always are not tangent to the sonic line (the characteristics can be defined up to the sonic line, which is also why we classify the EdGB equations as Tricomi type here [1, 2]). Thus excising on the sonic line should be fine, as long as it remains within the horizon.

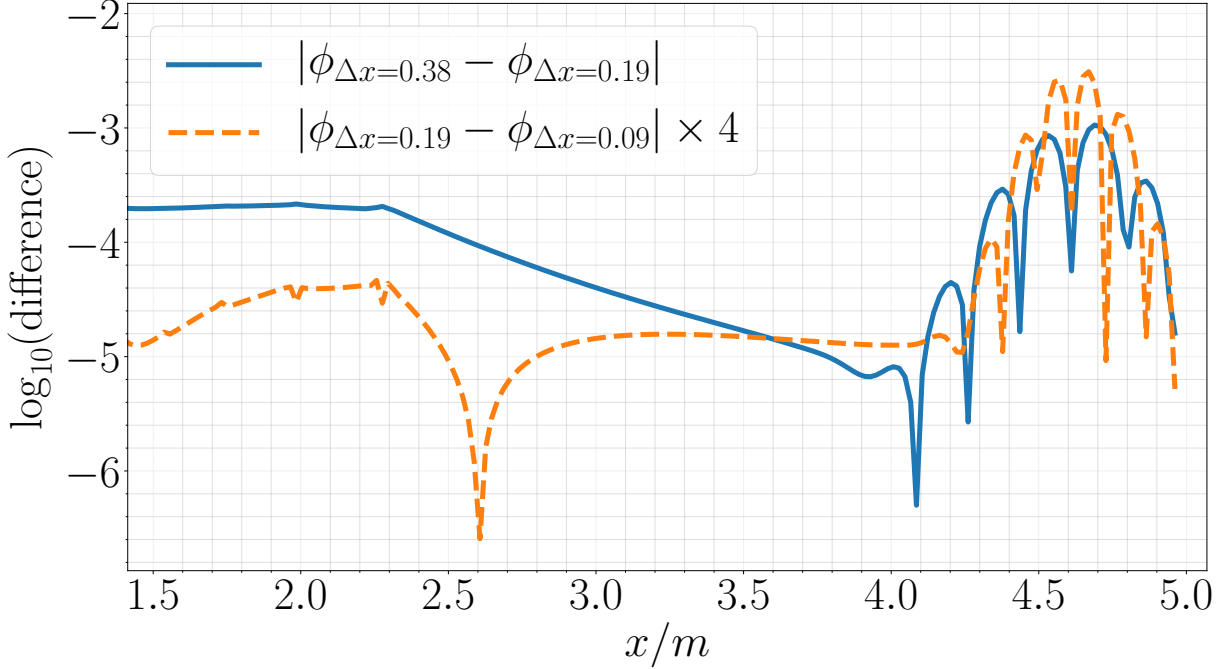
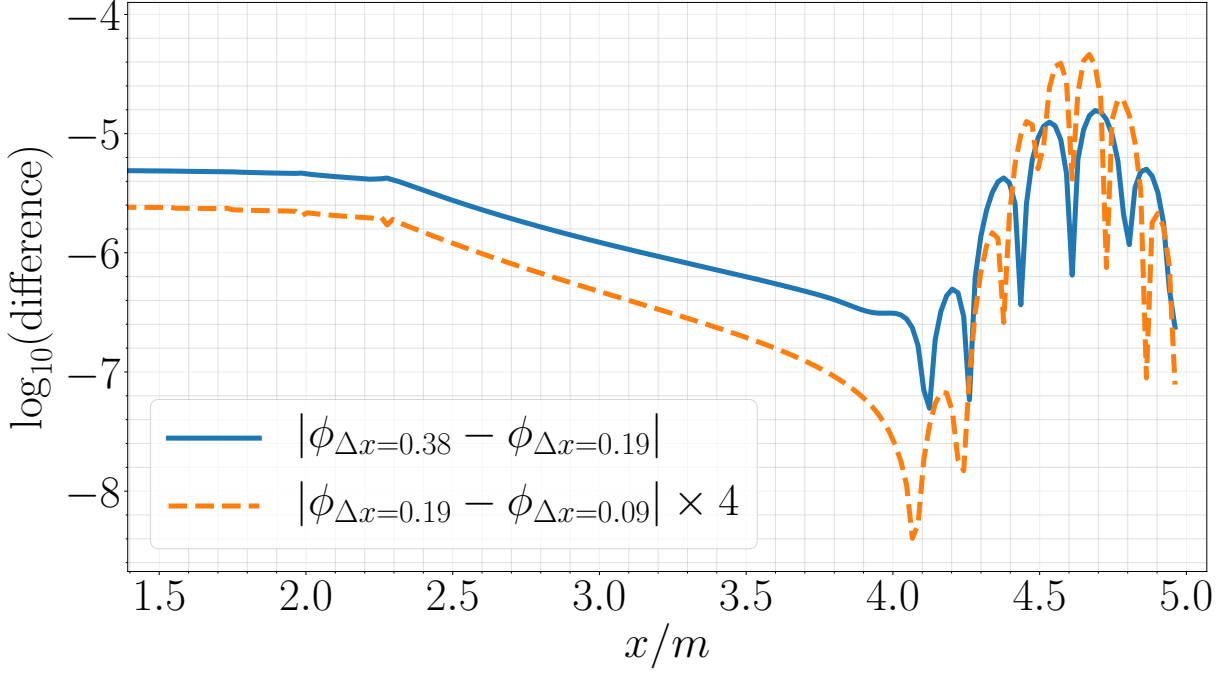


FIG. 4: Convergence and truncation error estimate at  $t \sim 100m$  for the scalar field  $\phi$ . Shown are point-wise differences of the solution computed with different resolutions; the decrease going to successively higher resolutions is consistent with second order convergence, and the magnitude for a given pair is an estimate of the error in the scalar field profile at those resolutions. Comparing with Fig. 3, we see we can resolve the difference of the scalar field from the decoupled value well above truncation error for the range of curvature-couplings considered here. We rescale the smaller truncation error estimate by 4, which is the expected convergence rate of our code based on the order of the second order finite difference stencils we use. For simulation parameters see Table. I.

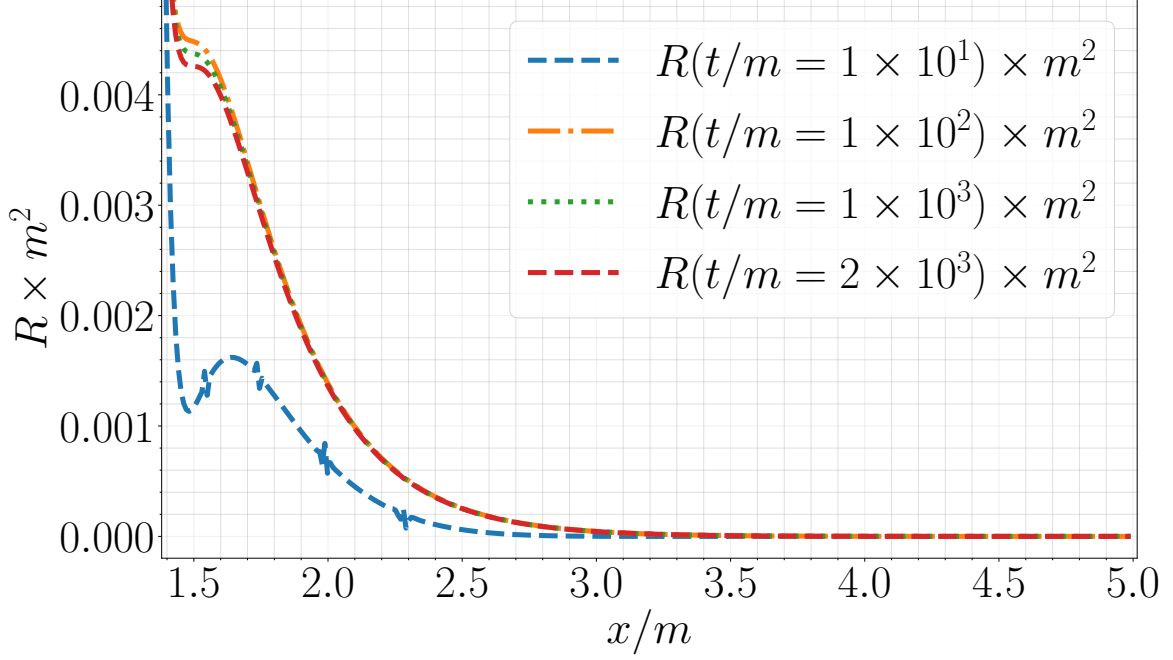


FIG. 5: Evolution of the Ricci scalar for the case  $C = 0.16$ ; see Fig.2 for evolution of the scalar field for this same simulation. The small “features” in the Ricci scalar at the  $t = 10m$  time slice are located at grid refinement boundaries, and converge away with higher base resolution (compare with Fig. 6). For simulation parameters see Table. I.

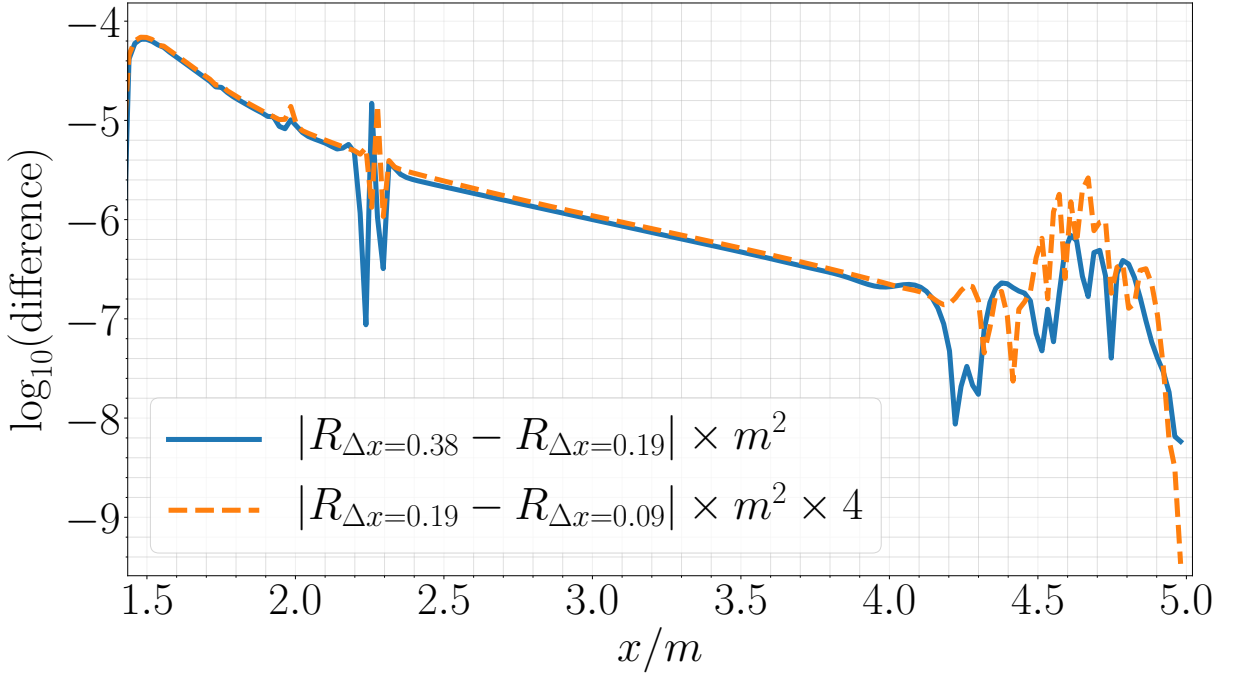


FIG. 6: Convergence and truncation error estimate at  $t \sim 100m$  for the Ricci scalar  $R$ , for the  $C = 0.16$  case (see Fig. 4 for a similar plot of the scalar field  $\phi$  for this case, and the caption there for a discussion of the error estimates). The oscillations near  $x/m \sim 2.3$  are at grid refinement boundary. We rescale the smaller truncation error estimate by 4, which is the expected convergence rate of our code based on the order of the second order finite difference stencils we use. For simulation parameters see Table. I.

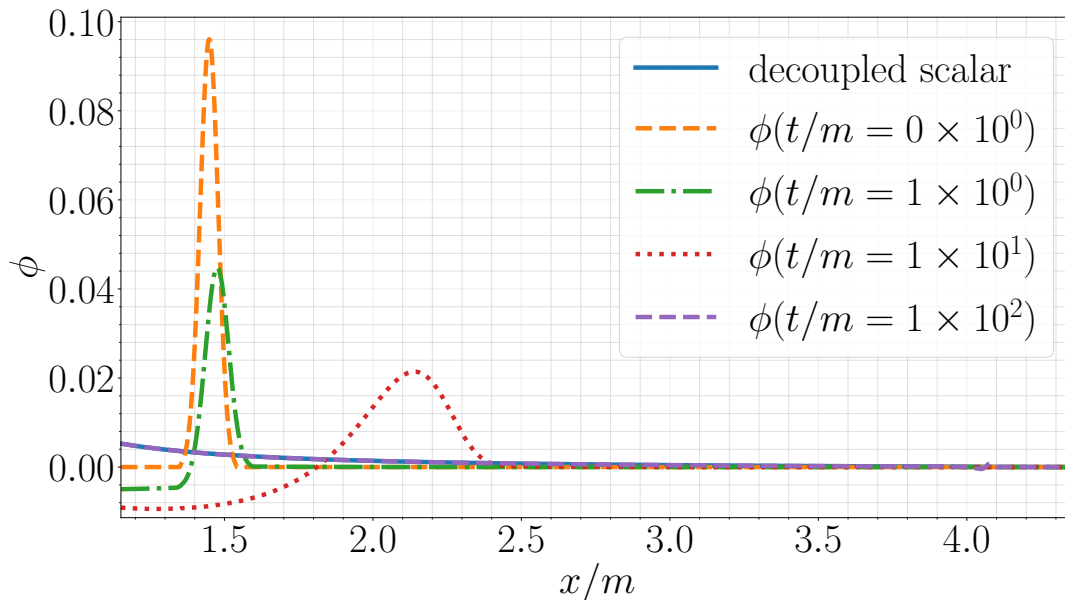


FIG. 7: Schwarzschild initial data perturbed by an EdGB scalar bump (see Eq. (27a)) outside the horizon. The mass of the initial Schwarzschild black hole is  $m_s = 20$ , while the scalar bump adds an additional  $\sim 3$  in mass, giving a net mass  $m = 23$ ; thus with  $\lambda = 1$  the curvature coupling is  $C = \lambda/m^2 \approx 2 \times 10^{-3}$ . Some of the scalar field falls into the black hole, while some disperses to infinity, and at late times the scalar field approaches the decoupled scalar field profile. For simulation parameters see Table. I.

and the location of the sonic line is at the zero of the discriminant,  $\mathcal{D} \equiv \mathcal{B}^2 - 4\mathcal{A}\mathcal{C}$ . After excising, if  $\mathcal{D}$  becomes positive definite within the computational domain, we estimate the location of the sonic line as the zero of a quadratic polynomial fitted to the function

$$c_+ - c_- = \frac{1}{\mathcal{A}} \sqrt{\mathcal{B}^2 - 4\mathcal{A}\mathcal{C}}, \quad (30)$$

using a set of points adjacent to the excision boundary. In typical cases for Schwarzschild initial data, and subextremal curvature couplings, this estimate suggests the true location of the final stationary sonic line lies within  $\sim 94\%$  of its maximum value (the excision point); see Fig. 8 for a survey of the late time values of the excision radius, MOTS location and sonic line estimate, and Fig. 9, for the evolution of these quantities for one example (including several resolutions). In the latter figure, the shrinking of the MOTS after some initial growth coincides with violation of the null convergence condition ( $R_{\mu\nu}k^\mu k^\nu \geq 0$  for all null vectors  $k^\mu$ ; see e.g. [49]), which is known to occur in EdGB gravity (for more details in the spherical collapse problem see [2]). A plot of  $R_{\mu\nu}k^\mu k^\nu$  is shown in Fig. 10. We note that the stable violation of the Null Convergence Condition (NCC) is thought to be a key ingredient in the construction of singularity free cosmological and black hole solutions (for a review, see e.g. [50]). This violation of the NCC appears to be transient: as the scalarized black hole settles to a stationary solution, we find the horizon stops shrinking and the region of NCC violation disappears. The slow increase in the horizon size for  $t/m \gtrsim 50$  is due to numerical error; we find it converges to zero with increasing resolution.

For curvature couplings above  $C_{extr}$ , the sonic line can move outside the MOTS, or initially appear outside it. Linearly extrapolating the data shown in Fig.8 to the location where the late time MOTS will cross the sonic line, we estimate  $C_{extr} \sim 0.23$ , close to but slightly larger than the value  $C_{extr} \sim 0.22$  coming from seeking exactly static EdGB black hole solutions with a non-singular  $\phi$  field on the horizon[5] (though even beyond caveats with our extrapolations, we do not expect these two methods to give identical numerical values for an extremal coupling). In Fig. 11 we show an example evolution of Schwarzschild initial data with superextremal curvature coupling. We see the sonic line quickly overtakes the black hole horizon, leading to a “naked” elliptic region.

## V. DISCUSSION

In this article we have presented numerical evidence that in spherical symmetry, and for sufficiently small curvature couplings (what we call subextremal), EdGB black holes are nonlinearly stable. For subextremal couplings even

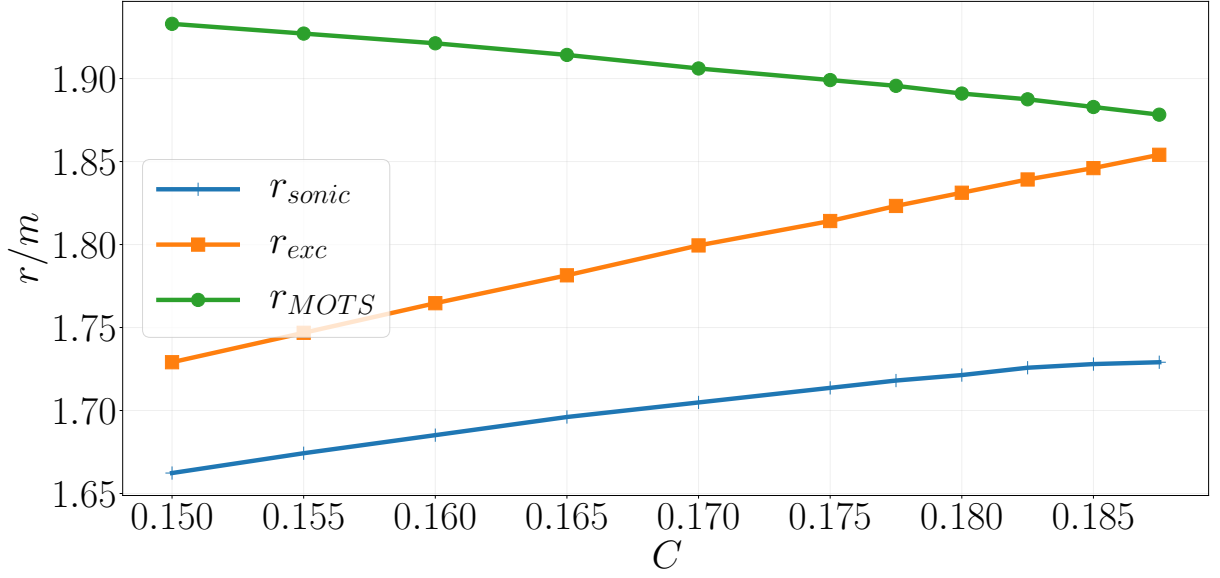


FIG. 8: The location of the MOTS  $r_{MOTS}$ , excision radius  $r_{exc}$ , and *estimated* sonic line position  $r_{sonic}$ , as a function of the curvature coupling  $C$ , measured at  $t \sim 80m$  during the evolution of Schwarzschild initial data, which is sufficiently late to give a good estimate of their static end state values (see Fig. 9). Due to our high water mark excision strategy, the excision point represents the largest measured radius the sonic line attained during evolution. Extrapolating the curves for the MOTS and sonic lines, we estimate the “extremal” coupling for our initial data to be  $C_{extr} \sim 0.23$ . These results were obtained with unigrid evolution using  $\Delta x = 0.012$  (corresponding to the highest resolution curves shown in Fig. 9). For  $C \geq 0.17$  runs the CFL number was 0.2, while for  $C < 0.17$  the CFL number was 0.1. For other simulation parameters see Table. I.

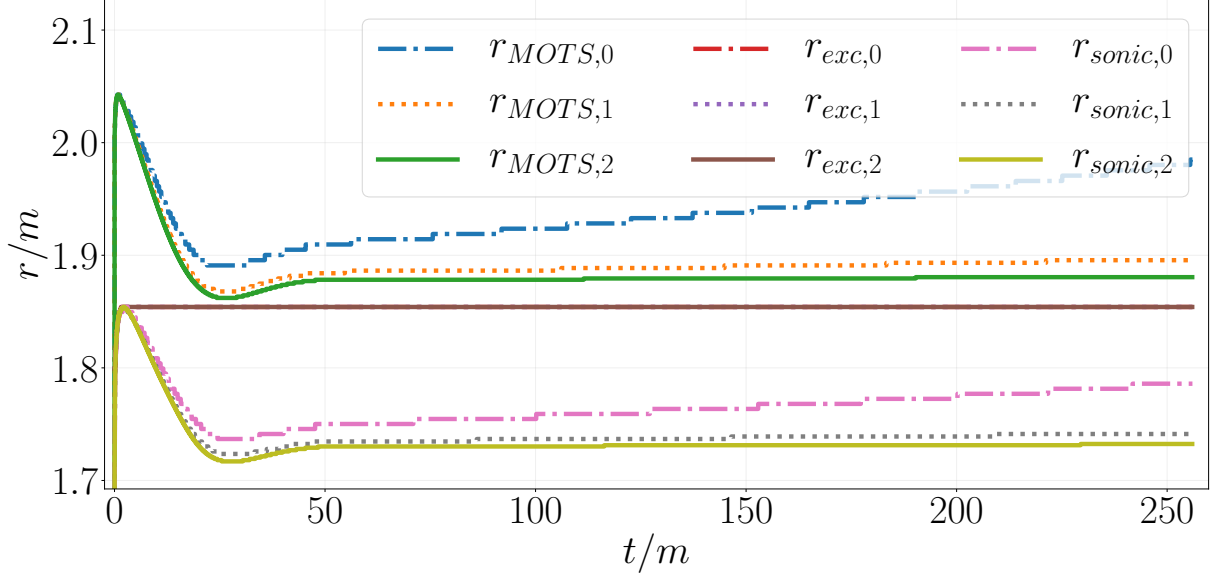


FIG. 9: Evolution of the MOTS, excision point, and sonic line as a function of time, for curvature coupling  $C = 0.1875$  (c.f. Fig. 8), and from runs at three resolutions : the labels 0, 1, 2 refer to unigrid resolutions  $\Delta x = 0.049$ ,  $\Delta x = 0.024$ , and  $\Delta x = 0.012$ , respectively (a CFL factor of 0.2 was used in all cases). At early times as the sonic line grows, we increase the location of the excision surface to match; after reaching a maximum radius, the sonic line presumably starts to shrink again, and then the curves in the figure show an estimate of this location based on extrapolation of the characteristic speeds (see Sec. IV D). The resolution study demonstrates that at late times we are converging to a static solution (in the vicinity of the horizon). For other run parameters see Table. I.

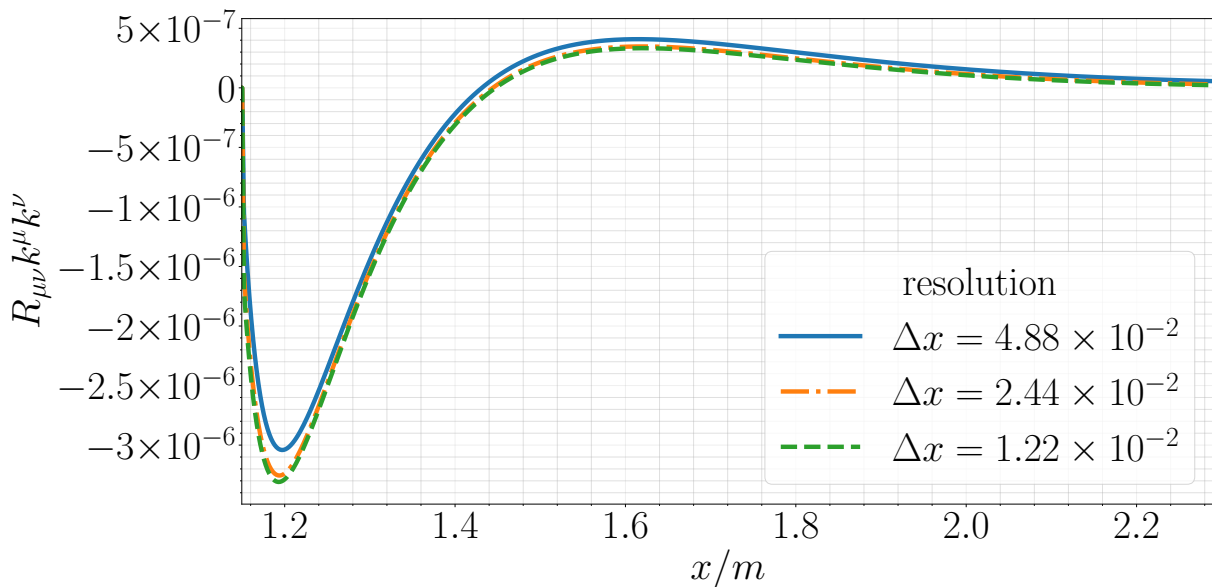


FIG. 10: Ricci tensor contracted with outgoing null vector  $k^\mu = (1, \alpha(-1 + \zeta), 0, 0)$  ( $R_{\mu\nu}k^\mu k^\nu$ ) at time  $t/m = 14$ . The curvature coupling  $C = 0.16$ . We see that the null convergence factor is not positive definite; where it is negative indicates a region of NCC violation. The region of NCC violation is localized near the black hole horizon and region of strongest scalar field growth. This resolution study demonstrates we can resolve the stable violation of the null convergence condition in EdGB gravity during the formation of a scalarized black hole solution. For simulation parameters see Table. I.

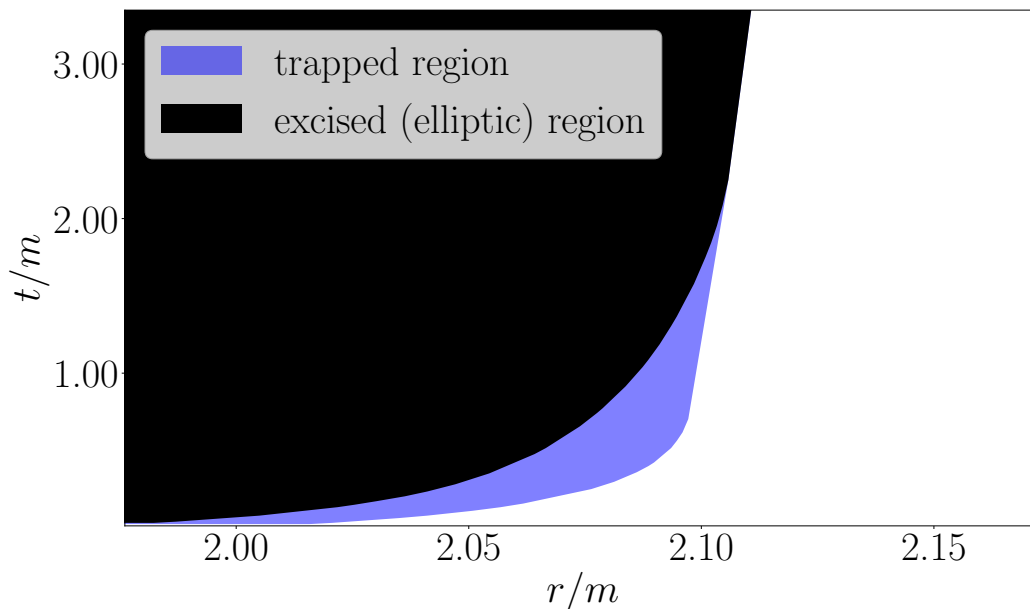


FIG. 11: Example evolution of Schwarzschild initial data with superextremal curvature coupling:  $C = 0.275$ . We excise along the sonic line, so the excised region can be thought of as the elliptic region. The sonic line very quickly reaches and overtakes the MOTS, and the elliptic region subsequently becomes “naked”, shortly after which the code crashes. We note our code crashes if we do not excise the elliptic region, regardless if it is interior or exterior to the black hole horizon. For simulation parameters see Table. I.

moderately close to the extremal limit, solving the decoupled scalar equation for the scalar field profile provides a good fit to the numerical solution obtained in the full theory. Beginning from Schwarzschild initial data, instead of developing a non-central curvature singularity in the interior as was found for static solutions [5], we find the formation of a sonic line and elliptic region in the interior. Our treatment of the EdGB equations as hyperbolic does not allow us to conclude anything about possible extensions of the spacetime into the elliptic region. For subextremal black holes, our statement about their stability relates to the region exterior to the horizon, and assumes that our excision strategy used to eliminate the interior elliptic region is self-consistent (which is supported by the stability/convergence of the corresponding numerical evolutions). For superextremal cases, the sonic line forms or evolves to be outside the horizon, meaning we cannot excise it, and we would need to treat the exterior equations as mixed-type to obtain sensible solutions (or said another way, then the exterior evolution ceases to satisfy a well-posed Cauchy initial value problem). The particular value of the curvature coupling we find for the extremal limit is similar to, but slightly different from that given for static EdGB black holes solutions [3, 5]; this is not particularly surprising given we are dynamically forming them from Schwarzschild initial data.

There are various ways in which this work could be extended. One is to explore a wider class of initial conditions; for example, collapse to a black hole from a regular matter source, whether the pure EdGB scalar field as in [2], or coupled to another source of matter driving most of the collapse (e.g. extending the study of [28], which only considered the decoupled EdGB field on top of Oppenheimer-Snyder style collapse, to the full EdGB equations). Recent work suggests that whether or not scalarized black holes form in the theory depends on the functional form of  $f(\phi)$  (see Eq. (1)) [6, 51]; with the methods presented in this paper one could explore these questions with numerical solutions to the full theory in spherical symmetry. Another future direction is to study critical collapse in EdGB gravity using adaptive mesh refinement.

Finally, this work could be extended by considering numerical solutions of EdGB gravity in axisymmetry, or without any symmetry restrictions. This would couple in propagating metric degrees of freedom, and hence introduce a qualitatively different aspect of the theory not available in spherical symmetry. If, similar to the conclusions found here and in [1, 2], there exist subsets of initial data that offer well-posed hyperbolic evolution, then EdGB gravity may still be viable as an interesting modified gravity theory to confront with gravitational wave binary merger data. On the other hand, if the linear analysis in [15, 16] that EdGB gravity is generically ill-posed in a particular gauge applies to all gauges, then the well-posed cases we have found could be an artifact of spherical symmetry, and including any gravitational wave degrees of freedom would render the theory ill-posed.

## ACKNOWLEDGMENTS

We thank Leo Stein for several encouraging discussions while this project was underway, and the anonymous referee for their helpful comments on an earlier draft of this paper. Computational resources were provided courtesy of the Feynman cluster at Princeton University. F.P. acknowledges support from NSF grant PHY-1912171, the Simons Foundation, and the Canadian Institute For Advanced Research (CIFAR).

### Appendix A: Convergence of an independent residual

In Fig. (12) we present the two norm of the  $E_{\theta\theta}$  component of the equation of motion for a representative case, excising the elliptic region, and evolved with fixed mesh refinement. We see second order convergence to zero over the entire run-time  $t \approx 2 \times 10^3 m$  of the simulation. The plot only shows the norm computed on the coarsest level, although we observe second order convergence over all levels of fixed mesh refinement (four in addition to the base level). As an example of how this translates to solution error, for the highest resolution case shown in Fig.12, after the early time transient behavior and the solution has settled to be nearly static at the horizon (see Fig.9), we see a net drift in the mass of the black hole of  $\delta m/m \sim 0.4\%$  over the remainder of the simulation. Other curvature couplings give similar results. If we do not excise the elliptic region we begin to lose convergence there, and eventually the code crashes, as expected.

### Appendix B: Decoupled EdGB scalarized black hole solutions

For reference, we present the decoupled scalar solutions for EdGB gravity in PG coordinates. The decoupling limit for EdGB gravity is the solution of the scalar wave equation

$$\square\phi + \lambda\mathcal{R}_{GB} = 0, \tag{B1}$$



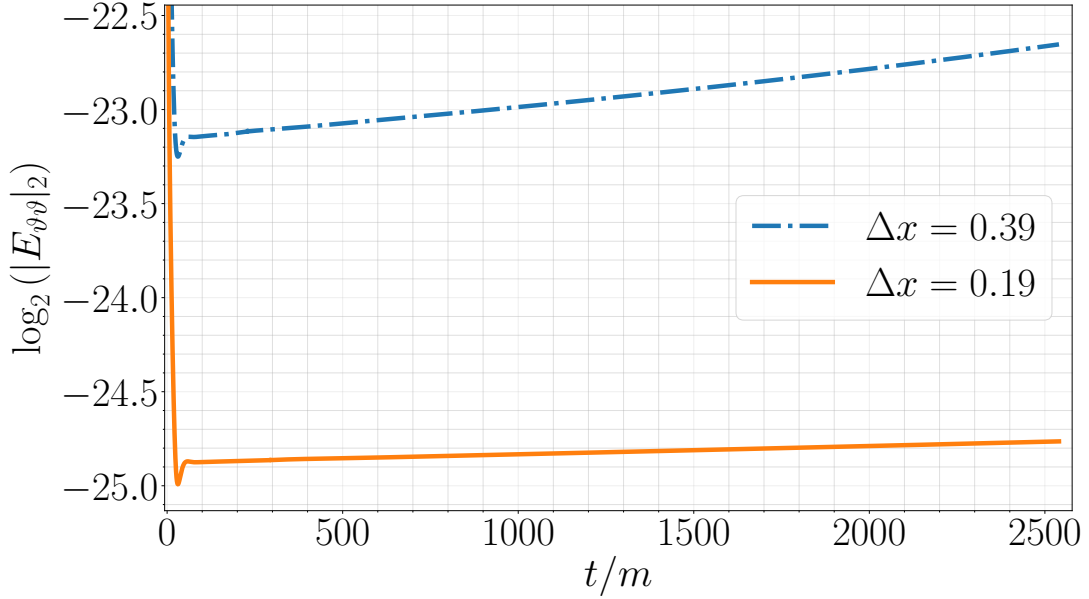


FIG. 12: Second order convergence to zero of the  $\vartheta\vartheta$  component of the equation of motion (3a) from a representative run: Schwarzschild black hole initial data, and curvature coupling  $C = 0.16$ . Shown is  $\log_2(|E_{\vartheta\vartheta}|_2)$  versus time computed on the base level of a fixed mesh refinement run (other levels also show second order convergence to zero). The  $\log_2$  is chosen so the second order convergence is more apparent. For simulation parameters see Table. I.

about a GR background. Our background is the Schwarzschild spacetime:

$$\alpha = 1, \quad \zeta = \sqrt{\frac{2m}{r}}. \quad (\text{B2})$$

We assume a static solution,  $\phi(r)$ , for which Eq. (B1) becomes

$$\frac{1}{r^2} \frac{d}{dr} \left( r^2 \left( 1 - \frac{2m}{r} \right) \frac{d\phi}{dr} \right) + \frac{48\lambda m^2}{r^6} = 0. \quad (\text{B3})$$

The solution to this equation is

$$\phi(r) = \frac{2\lambda}{m} \frac{1}{r} + 2\lambda \frac{1}{r^2} + \frac{8m\lambda}{3} \frac{1}{r^3} + \frac{c_1 m + 2\lambda}{2m^2} \log \left( 1 - \frac{2m}{r} \right) + c_2, \quad (\text{B4})$$

where  $c_1$  and  $c_2$  are integration constants. Regularity at the black hole horizon sets  $c_1 = -2\lambda/m$ , and requiring  $\phi(r = \infty) = 0$  sets  $c_2 = 0$ . We have

$$\phi(r) = \frac{2\lambda}{m^2} \left( \frac{m}{r} + \frac{m^2}{r^2} + \frac{4}{3} \frac{m^3}{r^3} \right), \quad (\text{B5})$$

which is the solution we compare our numerical results against in this article. Note from [17] that the dynamical solution to Eq. (B1) has been shown to asymptotically settle to the static solution (B5) for Schwarzschild backgrounds.

### Appendix C: Form of functions $\mathcal{A}_{(P)}\mathcal{F}_{(P)}$ , $\mathcal{A}_{(\zeta)}$ , and $\mathcal{F}_{(\zeta)}$

Here we provide the (lengthy) expressions for the functions  $\mathcal{A}_{(P)}$  and  $\mathcal{F}_{(P)}$ , (see Eq. (7b)),  $\mathcal{A}_{(\zeta)}$ , and  $\mathcal{F}_{(\zeta)}$  (see Eq. (22)), which we produced using Mathematica [52]. While we work only for  $f(\phi) = \phi$  in this article, we show the complete expressions for reference.

$$\mathcal{A}_{(P)} \equiv 1 + \left( -\frac{16\lambda Q}{r} - \frac{16\lambda P\zeta}{r} \right) f' + \left( \frac{64\lambda^2 Q^2}{r^2} + \frac{128\lambda^2 P Q \zeta}{r^2} + \frac{64\lambda^2 P^2 \zeta^2}{r^2} - \frac{32\lambda^2 \zeta^4}{r^4} \right) (f')^2$$

$$\begin{aligned}
& + \frac{256\lambda^3 Q^2 \zeta^4 (f')^2 f''}{r^4} + \frac{256\lambda^3 \zeta^4 (f')^3 \partial_r Q}{r^4} + \left( \frac{128\lambda^2 \zeta^4 (f')^2}{r^3 \alpha} + \left( -\frac{1024\lambda^3 Q \zeta^4}{r^4 \alpha} - \frac{768\lambda^3 P \zeta^5}{r^4 \alpha} \right) (f')^3 \right) \partial_r \alpha \\
& + \left( \frac{128\lambda^2 \zeta^3 (f')^2}{r^3} + \left( -\frac{1024\lambda^3 Q \zeta^3}{r^4} - \frac{768\lambda^3 P \zeta^4}{r^4} \right) (f')^3 \right) \partial_r \zeta, \tag{C1a} \\
\mathcal{F}_{(P)} \equiv & -\frac{2Q\alpha}{r} - \frac{2P\alpha\zeta}{r} + \left( \frac{32\lambda Q^2 \alpha}{r^2} + \frac{60\lambda P Q \alpha \zeta}{r^2} + \frac{34\lambda P^2 \alpha \zeta^2}{r^2} - \frac{6\lambda Q^2 \alpha \zeta^2}{r^2} - \frac{4\lambda \alpha \zeta^4}{r^4} \right) f' \\
& + \left( -\frac{128\lambda^2 Q^3 \alpha}{r^3} - \frac{384\lambda^2 P Q^2 \alpha \zeta}{r^3} - \frac{416\lambda^2 P^2 Q \alpha \zeta^2}{r^3} + \frac{32\lambda^2 Q^3 \alpha \zeta^2}{r^3} - \frac{160\lambda^2 P^3 \alpha \zeta^3}{r^3} + \frac{32\lambda^2 P Q^2 \alpha \zeta^3}{r^3} \right) (f')^2 \\
& + \left( \frac{32\lambda^2 P Q^3 \alpha \zeta}{r^2} + \frac{16\lambda^2 P^2 Q^2 \alpha \zeta^2}{r^2} + \frac{16\lambda^2 Q^4 \alpha \zeta^2}{r^2} - \frac{32\lambda^2 P Q \alpha \zeta^3}{r^4} - \frac{32\lambda^2 P^2 \alpha \zeta^4}{r^4} + \frac{32\lambda^2 Q^2 \alpha \zeta^4}{r^4} \right) f' f'' \\
& + \left( \frac{256\lambda^3 P Q^3 \alpha \zeta^3}{r^4} + \frac{256\lambda^3 P^2 Q^2 \alpha \zeta^4}{r^4} \right) f' (f'')^2 \\
& + \left( -\alpha + \left( \frac{16\lambda Q \alpha}{r} + \frac{16\lambda P \alpha \zeta}{r} \right) f' \right. \\
& + \left( -\frac{64\lambda^2 Q^2 \alpha}{r^2} - \frac{96\lambda^2 P Q \alpha \zeta}{r^2} - \frac{48\lambda^2 P^2 \alpha \zeta^2}{r^2} + \frac{16\lambda^2 Q^2 \alpha \zeta^2}{r^2} + \frac{32\lambda^2 \alpha \zeta^4}{r^4} \right) (f')^2 \\
& + \left. \left( \frac{256\lambda^3 P Q \alpha \zeta^3}{r^4} + \frac{256\lambda^3 P^2 \alpha \zeta^4}{r^4} \right) (f')^2 f'' \right) \partial_r Q \\
& + \left( -\alpha \zeta + \left( \frac{16\lambda Q \alpha \zeta}{r} + \frac{16\lambda P \alpha \zeta^2}{r} \right) f' \right. \\
& + \left( -\frac{64\lambda^2 Q^2 \alpha \zeta}{r^2} - \frac{128\lambda^2 P Q \alpha \zeta^2}{r^2} - \frac{32\lambda^2 \alpha \zeta^3}{r^4} - \frac{64\lambda^2 P^2 \alpha \zeta^3}{r^2} + \frac{32\lambda^2 \alpha \zeta^5}{r^4} \right) (f')^2 \\
& + \left. \left( \frac{256\lambda^3 Q^2 \alpha \zeta^3}{r^4} - \frac{256\lambda^3 Q^2 \alpha \zeta^5}{r^4} \right) (f')^2 f'' + \left( \frac{256\lambda^3 \alpha \zeta^3}{r^4} - \frac{256\lambda^3 \alpha \zeta^5}{r^4} \right) (f')^3 \partial_r Q \right) \partial_r P \\
& + \left( \left( \frac{64\lambda^2 P \zeta^3}{r^3 \alpha} + \frac{64\lambda^2 Q \zeta^4}{r^3 \alpha} \right) (f')^2 \right. \\
& + \left. \left( -\frac{512\lambda^3 P Q \zeta^3}{r^4 \alpha} - \frac{512\lambda^3 P^2 \zeta^4}{r^4 \alpha} - \frac{512\lambda^3 Q^2 \zeta^4}{r^4 \alpha} - \frac{512\lambda^3 P Q \zeta^5}{r^4 \alpha} \right) (f')^3 \right) (\partial_r \alpha)^2 \\
& + \left( -P\alpha + \left( \frac{24\lambda P Q \alpha}{r} + \frac{20\lambda P^2 \alpha \zeta}{r} + \frac{4\lambda Q^2 \alpha \zeta}{r} + \frac{16\lambda \alpha \zeta^3}{r^3} \right) f' \right. \\
& + \left( -\frac{128\lambda^2 P Q^2 \alpha}{r^2} - \frac{192\lambda^2 P^2 Q \alpha \zeta}{r^2} - \frac{32\lambda^2 Q^3 \alpha \zeta}{r^2} - \frac{80\lambda^2 P^3 \alpha \zeta^2}{r^2} - \frac{16\lambda^2 P Q^2 \alpha \zeta^2}{r^2} - \frac{160\lambda^2 Q \alpha \zeta^3}{r^4} - \frac{96\lambda^2 P \alpha \zeta^4}{r^4} \right) (f')^2 \\
& + \left( \left( \frac{64\lambda^2 P Q \alpha \zeta^2}{r^3} + \frac{128\lambda^2 P^2 \alpha \zeta^3}{r^3} \right) f' + \left( -\frac{512\lambda^3 P Q^2 \alpha \zeta^2}{r^4} - \frac{1280\lambda^3 P^2 Q \alpha \zeta^3}{r^4} + \frac{256\lambda^3 Q^3 \alpha \zeta^3}{r^4} - \frac{768\lambda^3 P^3 \alpha \zeta^4}{r^4} \right) (f')^2 \right) f'' \\
& + \left( \left( \frac{64\lambda^2 \alpha \zeta^2}{r^3} - \frac{128\lambda^2 \alpha \zeta^4}{r^3} \right) (f')^2 + \left( -\frac{512\lambda^3 Q \alpha \zeta^2}{r^4} - \frac{256\lambda^3 P \alpha \zeta^3}{r^4} + \frac{1024\lambda^3 Q \alpha \zeta^4}{r^4} + \frac{768\lambda^3 P \alpha \zeta^5}{r^4} \right) (f')^3 \right) \partial_r P \\
& + \left. \frac{256\lambda^3 Q \alpha \zeta^3 (f')^3 \partial_r Q}{r^4} \right) \partial_r \zeta \\
& + \left( \frac{64\lambda^2 Q \alpha \zeta^2 (f')^2}{r^3} + \left( -\frac{512\lambda^3 Q^2 \alpha \zeta^2}{r^4} - \frac{256\lambda^3 P Q \alpha \zeta^3}{r^4} \right) (f')^3 \right) (\partial_r \zeta)^2 \\
& + \left( -Q - P\zeta + \left( \frac{16\lambda Q^2}{r} + \frac{40\lambda P Q \zeta}{r} - \frac{8\lambda \zeta^2}{r^3} + \frac{20\lambda P^2 \zeta^2}{r} + \frac{4\lambda Q^2 \zeta^2}{r} + \frac{16\lambda \zeta^4}{r^3} \right) f' \right.
\end{aligned}$$

$$\begin{aligned}
& + \left( -\frac{64\lambda^2 Q^3}{r^2} - \frac{256\lambda^2 P Q^2 \zeta}{r^2} + \frac{64\lambda^2 Q \zeta^2}{r^4} - \frac{256\lambda^2 P^2 Q \zeta^2}{r^2} - \frac{32\lambda^2 Q^3 \zeta^2}{r^2} + \frac{64\lambda^2 P \zeta^3}{r^4} - \frac{80\lambda^2 P^3 \zeta^3}{r^2} \right. \\
& \left. - \frac{16\lambda^2 P Q^2 \zeta^3}{r^2} - \frac{128\lambda^2 Q \zeta^4}{r^4} - \frac{96\lambda^2 P \zeta^5}{r^4} \right) (f')^2 \\
& + \left( \left( \frac{64\lambda^2 Q^2 \zeta^2}{r^3} + \frac{192\lambda^2 P Q \zeta^3}{r^3} + \frac{128\lambda^2 P^2 \zeta^4}{r^3} \right) f' \right. \\
& + \left( -\frac{512\lambda^3 Q^3 \zeta^2}{r^4} - \frac{2048\lambda^3 P Q^2 \zeta^3}{r^4} - \frac{2304\lambda^3 P^2 Q \zeta^4}{r^4} - \frac{768\lambda^3 P^3 \zeta^5}{r^4} \right) (f')^2 \Big) f'' \\
& + \left( \left( \frac{192\lambda^2 \zeta^3}{r^3} - \frac{128\lambda^2 \zeta^5}{r^3} \right) (f')^2 + \left( -\frac{1536\lambda^3 Q \zeta^3}{r^4} - \frac{1280\lambda^3 P \zeta^4}{r^4} + \frac{1024\lambda^3 Q \zeta^5}{r^4} + \frac{768\lambda^3 P \zeta^6}{r^4} \right) (f')^3 \right) \partial_r P \\
& + \left( \frac{64\lambda^2 \zeta^2 (f')^2}{r^3} + \left( -\frac{512\lambda^3 Q \zeta^2}{r^4} - \frac{512\lambda^3 P \zeta^3}{r^4} \right) (f')^3 \right) \partial_r Q \\
& + \left( \frac{16\lambda \zeta f'}{r^2} + \left( -\frac{256\lambda^2 Q \zeta}{r^3} - \frac{192\lambda^2 P \zeta^2}{r^3} + \frac{128\lambda^2 Q \zeta^3}{r^3} \right) (f')^2 \right. \\
& \left. + \left( \frac{1024\lambda^3 Q^2 \zeta}{r^4} + \frac{1536\lambda^3 P Q \zeta^2}{r^4} + \frac{512\lambda^3 P^2 \zeta^3}{r^4} - \frac{1024\lambda^3 Q^2 \zeta^3}{r^4} - \frac{768\lambda^3 P Q \zeta^4}{r^4} \right) (f')^3 \right) \partial_r \zeta \Big) \partial_r \alpha, \tag{C1b}
\end{aligned}$$

$$\begin{aligned}
\mathcal{A}_{(\zeta)} & = 1 + \left( -\frac{16\lambda Q}{r} - \frac{16\lambda P \zeta}{r} \right) f' + \left( \frac{64\lambda^2 Q^2}{r^2} + \frac{128\lambda^2 P Q \zeta}{r^2} + \frac{64\lambda^2 P^2 \zeta^2}{r^2} - \frac{32\lambda^2 \zeta^4}{r^4} \right) (f')^2 \\
& + \frac{256\lambda^3 Q^2 \zeta^4 (f')^2 f''}{r^4} + \frac{256\lambda^3 \zeta^4 (f')^3 \partial_r Q}{r^4} + \left( \frac{128\lambda^2 \zeta^4 (f')^2}{r^3 \alpha} + \left( -\frac{1024\lambda^3 Q \zeta^4}{r^4 \alpha} - \frac{768\lambda^3 P \zeta^5}{r^4 \alpha} \right) (f')^3 \right) \partial_r \alpha \\
& + \left( \frac{128\lambda^2 \zeta^3 (f')^2}{r^3} + \left( -\frac{1024\lambda^3 Q \zeta^3}{r^4} - \frac{768\lambda^3 P \zeta^4}{r^4} \right) (f')^3 \right) \partial_r \zeta, \tag{C1c}
\end{aligned}$$

$$\begin{aligned}
\mathcal{F}_{(\zeta)} & = -\frac{1}{4} r P^2 \alpha - \frac{1}{4} r Q^2 \alpha - \frac{r P Q \alpha}{2\zeta} - \frac{\alpha \zeta^2}{2r} \\
& + \left( 6\lambda P^2 Q \alpha + 2\lambda Q^3 \alpha + \frac{4\lambda P Q^2 \alpha}{\zeta} + 2\lambda P^3 \alpha \zeta + 2\lambda P Q^2 \alpha \zeta - \frac{4\lambda Q \alpha \zeta^2}{r^2} - \frac{4\lambda P \alpha \zeta^3}{r^2} \right) f' \\
& + \left( \frac{64\lambda^2 Q^2 \alpha \zeta^2}{r^3} + \frac{128\lambda^2 P Q \alpha \zeta^3}{r^3} + \frac{80\lambda^2 P^2 \alpha \zeta^4}{r^3} - \frac{16\lambda^2 Q^2 \alpha \zeta^4}{r^3} \right) (f')^2 \\
& + \left( -\frac{4\lambda P Q \alpha \zeta}{r} - \frac{4\lambda P^2 \alpha \zeta^2}{r} + \left( \frac{32\lambda^2 P Q^2 \alpha \zeta}{r^2} + \frac{64\lambda^2 P^2 Q \alpha \zeta^2}{r^2} + \frac{32\lambda^2 P^3 \alpha \zeta^3}{r^2} \right) f' \right) f'' \\
& + \left( -\frac{4\lambda \alpha \zeta f'}{r} + \left( \frac{32\lambda^2 Q \alpha \zeta}{r^2} + \frac{32\lambda^2 P \alpha \zeta^2}{r^2} \right) (f')^2 \right) \partial_r P \\
& + \left( -\frac{4\lambda \alpha \zeta^2 f'}{r} + \left( \frac{32\lambda^2 Q \alpha \zeta^2}{r^2} + \frac{32\lambda^2 P \alpha \zeta^3}{r^2} \right) (f')^2 \right) \partial_r Q \\
& + \left( \frac{256\lambda^3 P \zeta^5}{r^4 \alpha} + \frac{256\lambda^3 Q \zeta^6}{r^4 \alpha} \right) (f')^3 (\partial_r \alpha)^2 \\
& + \left( -\alpha \zeta + \left( \frac{12\lambda Q \alpha \zeta}{r} + \frac{12\lambda P \alpha \zeta^2}{r} \right) f' \right. \\
& + \left( -\frac{32\lambda^2 Q^2 \alpha \zeta}{r^2} - \frac{96\lambda^2 P Q \alpha \zeta^2}{r^2} - \frac{48\lambda^2 P^2 \alpha \zeta^3}{r^2} - \frac{16\lambda^2 Q^2 \alpha \zeta^3}{r^2} + \frac{32\lambda^2 \alpha \zeta^5}{r^4} \right) (f')^2 \\
& \left. + \left( -\frac{256\lambda^3 P Q \alpha \zeta^4}{r^4} - \frac{256\lambda^3 Q^2 \alpha \zeta^5}{r^4} \right) (f')^2 f'' - \frac{256\lambda^3 \alpha \zeta^4 (f')^3 \partial_r P}{r^4} - \frac{256\lambda^3 \alpha \zeta^5 (f')^3 \partial_r Q}{r^4} \right) \partial_r \zeta
\end{aligned}$$

$$\begin{aligned}
& + \left( -\frac{128\lambda^2\alpha\zeta^4(f')^2}{r^3} + \left( \frac{768\lambda^3Q\alpha\zeta^4}{r^4} + \frac{768\lambda^3P\alpha\zeta^5}{r^4} \right) (f')^3 \right) (\partial_r\zeta)^2 \\
& + \left( \left( -\frac{4\lambda Q\zeta^2}{r} - \frac{4\lambda P\zeta^3}{r} \right) f' + \left( \frac{32\lambda^2Q^2\zeta^2}{r^2} + \frac{32\lambda^2PQ\zeta^3}{r^2} - \frac{32\lambda^2\zeta^4}{r^4} + \frac{16\lambda^2P^2\zeta^4}{r^2} - \frac{16\lambda^2Q^2\zeta^4}{r^2} \right) (f')^2 \right. \\
& + \left. \left( \frac{256\lambda^3Q^2\zeta^4}{r^4} + \frac{256\lambda^3PQ\zeta^5}{r^4} \right) (f')^2 f'' + \frac{256\lambda^3\zeta^5(f')^3 \partial_r P}{r^4} + \frac{256\lambda^3\zeta^4(f')^3 \partial_r Q}{r^4} \right. \\
& + \left. \left( \left( \frac{64\lambda^2\zeta^3}{r^3} - \frac{128\lambda^2\zeta^5}{r^3} \right) (f')^2 + \left( -\frac{512\lambda^3Q\zeta^3}{r^4} - \frac{256\lambda^3P\zeta^4}{r^4} + \frac{1024\lambda^3Q\zeta^5}{r^4} + \frac{768\lambda^3P\zeta^6}{r^4} \right) (f')^3 \right) \partial_r\zeta \right) \partial_r\alpha. \quad (C1d)
\end{aligned}$$

- 
- [1] J. L. Ripley and F. Pretorius, Phys. Rev. **D99**, 084014 (2019), arXiv:1902.01468 [gr-qc].
- [2] J. L. Ripley and F. Pretorius, Class. Quant. Grav. **36**, 134001 (2019), arXiv:1903.07543 [gr-qc].
- [3] P. Kanti, N. E. Mavromatos, J. Rizos, K. Tamvakis, and E. Winstanley, Phys. Rev. **D54**, 5049 (1996), arXiv:hep-th/9511071 [hep-th].
- [4] T. P. Sotiriou and S.-Y. Zhou, Phys. Rev. Lett. **112**, 251102 (2014), arXiv:1312.3622 [gr-qc].
- [5] T. P. Sotiriou and S.-Y. Zhou, Phys. Rev. **D90**, 124063 (2014), arXiv:1408.1698 [gr-qc].
- [6] H. O. Silva, C. F. B. Macedo, T. P. Sotiriou, L. Gualtieri, J. Sakstein, and E. Berti, Phys. Rev. D **99**, 064011 (2019).
- [7] C. F. B. Macedo, J. Sakstein, E. Berti, L. Gualtieri, H. O. Silva, and T. P. Sotiriou, Phys. Rev. **D99**, 104041 (2019), arXiv:1903.06784 [gr-qc].
- [8] K. Yagi, L. C. Stein, and N. Yunes, Phys. Rev. **D93**, 024010 (2016), arXiv:1510.02152 [gr-qc].
- [9] B. P. Abbott *et al.* (LIGO Scientific, Virgo), Phys. Rev. Lett. **123**, 011102 (2019), arXiv:1811.00364 [gr-qc].
- [10] O. J. Tattersall, P. G. Ferreira, and M. Lagos, Phys. Rev. **D97**, 084005 (2018), arXiv:1802.08606 [gr-qc].
- [11] D. Ayzenberg, K. Yagi, and N. Yunes, Phys. Rev. **D89**, 044023 (2014), arXiv:1310.6392 [gr-qc].
- [12] N. Yunes, K. Yagi, and F. Pretorius, Phys. Rev. **D94**, 084002 (2016), arXiv:1603.08955 [gr-qc].
- [13] B. Zwiebach, Phys. Lett. **156B**, 315 (1985).
- [14] D. J. Gross and J. H. Sloan, Nucl. Phys. **B291**, 41 (1987).
- [15] G. Papallo and H. S. Reall, Phys. Rev. **D96**, 044019 (2017), arXiv:1705.04370 [gr-qc].
- [16] G. Papallo, Phys. Rev. **D96**, 124036 (2017), arXiv:1710.10155 [gr-qc].
- [17] R. Benkel, T. P. Sotiriou, and H. Witek, Phys. Rev. D **94**, 121503 (2016).
- [18] M. Okounkova, L. C. Stein, M. A. Scheel, and D. A. Hemberger, Phys. Rev. **D96**, 044020 (2017), arXiv:1705.07924 [gr-qc].
- [19] M. Okounkova, M. A. Scheel, and S. A. Teukolsky, Phys. Rev. **D99**, 044019 (2019), arXiv:1811.10713 [gr-qc].
- [20] H. Witek, L. Gualtieri, P. Pani, and T. P. Sotiriou, Phys. Rev. **D99**, 064035 (2019), arXiv:1810.05177 [gr-qc].
- [21] M. Okounkova, L. C. Stein, M. A. Scheel, and S. A. Teukolsky, Phys. Rev. **D100**, 104026 (2019), arXiv:1906.08789 [gr-qc].
- [22] M. Okounkova, (2019), arXiv:1909.12251 [gr-qc].
- [23] M. Okounkova, L. C. Stein, J. Moxon, M. A. Scheel, and S. A. Teukolsky, (2019), arXiv:1911.02588 [gr-qc].
- [24] W. Israel and J. M. Stewart, Annals Phys. **118**, 341 (1979).
- [25] J. Cayuso, N. Ortiz, and L. Lehner, Phys. Rev. **D96**, 084043 (2017), arXiv:1706.07421 [gr-qc].
- [26] G. Allwright and L. Lehner, Class. Quant. Grav. **36**, 084001 (2019), arXiv:1808.07897 [gr-qc].
- [27] T. Kobayashi, Rept. Prog. Phys. **82**, 086901 (2019), arXiv:1901.07183 [gr-qc].
- [28] R. Benkel, T. P. Sotiriou, and H. Witek, Class. Quant. Grav. **34**, 064001 (2017), arXiv:1610.09168 [gr-qc].
- [29] J. L. Blazquez-Salcedo, C. F. B. Macedo, V. Cardoso, V. Ferrari, L. Gualtieri, F. S. Khoo, J. Kunz, and P. Pani, Phys. Rev. **D94**, 104024 (2016), arXiv:1609.01286 [gr-qc].
- [30] C. S. Morawetz, Communications on Pure and Applied Mathematics **23**, 587 (1970), <https://onlinelibrary.wiley.com/doi/pdf/10.1002/cpa.3160230404>.
- [31] C. W. Misner, K. S. Thorne, and J. A. Wheeler, *Gravitation* (W. H. Freeman, San Francisco, 1973).
- [32] E. B. et. al., Classical and Quantum Gravity **32**, 243001 (2015).
- [33] R. J. Adler, J. D. Bjorken, P. Chen, and J. S. Liu, Am. J. Phys. **73**, 1148 (2005), arXiv:gr-qc/0502040 [gr-qc].
- [34] J. Ziprick and G. Kunstatter, Phys. Rev. D **79**, 101503 (2009).
- [35] Y. Kanai, M. Siino, and A. Hosoya, Prog. Theor. Phys. **125**, 1053 (2011), arXiv:1008.0470 [gr-qc].
- [36] J. L. Ripley, Class. Quant. Grav. **36**, 237001 (2019), arXiv:1908.04234 [gr-qc].
- [37] C. W. Misner and D. H. Sharp, Phys. Rev. **136**, B571 (1964).
- [38] H. Kodama, Prog. Theor. Phys. **63**, 1217 (1980).
- [39] H. Maeda and M. Nozawa, Phys. Rev. **D77**, 064031 (2008), arXiv:0709.1199 [hep-th].
- [40] G. Abreu and M. Visser, Phys. Rev. **D82**, 044027 (2010), arXiv:1004.1456 [gr-qc].
- [41] J. Thornburg, Living Reviews in Relativity **10**, 3 (2007).
- [42] T. Otway, *Elliptic-Hyperbolic Partial Differential Equations: A Mini-Course in Geometric and Quasilinear Methods*, SpringerBriefs in Mathematics (Springer International Publishing, 2015).
- [43] C. D. Leonard, J. Ziprick, G. Kunstatter, and R. B. Mann, JHEP **10**, 028 (2011), arXiv:1106.2054 [gr-qc].

- [44] R. Akhoury, D. Garfinkle, and R. Saotome, *JHEP* **04**, 096 (2011), arXiv:1103.0290 [gr-qc].
- [45] L. Bernard, L. Lehner, and R. Luna, *Phys. Rev.* **D100**, 024011 (2019), arXiv:1904.12866 [gr-qc].
- [46] M. J. Berger and J. Olinger, *Journal of Computational Physics* **53**, 484 (1984).
- [47] F. Pretorius and M. W. Choptuik, *J. Comput. Phys.* **218**, 246 (2006), arXiv:gr-qc/0508110 [gr-qc].
- [48] M. W. Choptuik, *A study of numerical techniques for radiative problems in general relativity*, Ph.D. thesis, University of British Columbia (1986).
- [49] S. W. Hawking and G. F. R. Ellis, *The Large Scale Structure of Space-Time (Cambridge Monographs on Mathematical Physics)* (Cambridge University Press, 1975).
- [50] V. A. Rubakov, *Phys. Usp.* **57**, 128 (2014), [*Usp. Fiz. Nauk*184,no.2,137(2014)], arXiv:1401.4024 [hep-th].
- [51] M. Minamitsuji and T. Ikeda, *Phys. Rev. D* **99**, 044017 (2019).
- [52] W. R. Inc., “Mathematica, Version 12.0,” .